

Department of Physics and Astronomy

University of Heidelberg

Master thesis in Physics

submitted by Dohun Kim

born in Gwangju

2020

Timing Study and Optimization of ATLASPix3

a full-scale HV-MAPS Prototype

This Master thesis has been carried out by Dohun Kim
at the Physikalisches Institut
under the supervision of
Herrn Prof. André Schöning

죽는 날까지 하늘을 우러러 한 점 부끄럼이 없기를.

앞새에 이는 바람에도 나는 괴로워 했다.

별을 노래하는 마음으로 모든 죽어가는것을 사랑해야지

그리고 나에게 주어진 길을 걸어가야 겠다

오늘 밤에도 별이 바람에 스치운다.

윤동주-서시

Abstract

ATLAS is one of the two LHC experiments that discovered the existence of the last key particle to complete the Standard Model, the Higgs boson. In order to measure properties of the Higgs boson more precisely and to search for potential signals of new physics, the HL-LHC upgrade is in preparation. For this upgrade, the Inner Detector will be replaced by an all-silicon tracking detector, the Inner Tracker (ITk). The requirements are a hit detection efficiency of 99 % and a time resolution of about 5 ns.

As a candidate for the outermost pixel layer, the ATLASPix3 was developed. It is a full scale prototype designed in an 180 nm HV-CMOS process by TSI. The pixel size is $150\ \mu\text{m} \times 50\ \mu\text{m}$, resulting in a matrix consisting of 132×372 pixels with a total active area of $19.8\ \text{mm} \times 18.6\ \text{mm}$.

This thesis focuses on the study and optimization of the time resolution of ATLASPix3. Different configurations are studied in the laboratory and then verified at testbeam campaigns. This strategy allows to draw conclusions on the efficiency and noise rate in connection with the achievable time resolution.

As a result of these measurements, a configuration is found which leads to an efficiency of 99.6 % with an uncorrected time resolution of (7.7 ± 0.1) ns. After offline correction, this value can be improved to (4.5 ± 0.1) ns.

Abstrakt

ATLAS ist eines der beiden LHC-Experimente, die die Existenz des letzten noch fehlenden Puzzleteils des Standardmodells der Teilchenphysik nachweisen konnten, des Higgs-Bosons. Um dessen Eigenschaften präzise vermessen und ebenfalls effizienter nach neuer Physik suchen zu können, befindet sich das HL-LHC-Upgrade in der Vorbereitung. In diesem Zusammenhang wird der innere Spurdetektor des ATLAS-Experiments durch einen ausschließlich aus Siliziumsensoren bestehenden Spurdetektor ersetzt, den sogenannten Inner Tracker (ITk). Die Anforderungen an diesen sind unter anderem eine Detektionseffizienz von 99 % und eine Zeitauflösung von ca. 5 ns in jeder Lage.

Als Kandidat für die äußerste Pixellage wurde der HV-MAPS-Prototyp ATLASPix3 entwickelt. Dieser wurde in einem 180 nm-HV-CMOS-Prozess von TSI produziert und er verfügt bereits über die finale Sensorgröße. Seine Pixelgröße beträgt $150\ \mu\text{m} \times 50\ \mu\text{m}$, was zusammen mit der Pixelanzahl von 132×372 die Größe der aktiven Fläche von $19.8\ \text{mm} \times 18.6\ \text{mm}$ ergibt.

Diese Arbeit behandelt die Untersuchung und Optimierung der Zeitauflösung von ATLASPix3. Verschiedene Sensorkonfigurationen werden im Labor untersucht und schließlich in Teststrahlkampagnen verifiziert. Dieses Vorgehen erlaubt es, Schlussfolgerungen über die beste erreichbare Zeitauflösung in Verbindung mit Ergebnissen zu Effizienz und Rauschen zu ziehen.

Mit der für eine hohe Zeitauflösung optimierten Sensorkonfiguration wird eine Effizienz von 99.6 % und eine Zeitauflösung von (7.7 ± 0.1) ns gemessen. Durch Offline-Korrekturen kann dieser Wert auf (4.5 ± 0.1) ns verbessert werden.

Contents

1	Introduction	13
1.1	Motivation	13
1.2	Standard Model	15
2	Particle Interaction with Matter	17
2.1	Charged Particles	17
2.1.1	Heavy Charged Particles	17
2.1.2	Electrons and Positrons	19
2.1.3	Bremsstrahlung	20
2.1.4	Multiple Coulomb Scattering	20
3	Pixel Detectors	21
3.1	Doping	21
3.2	PN-Junction	21
3.2.1	Signal Generation	23
3.3	Pixel Detectors	24
3.3.1	Hybrid Pixel Detectors	24
3.3.2	Monolithic Active Pixel Sensors (MAPS)	25
3.3.3	High Voltage MAPS (HV-MAPS)	25
4	ATLASPix3	27
4.1	Pixel Cell	28
4.2	Periphery Cell	30
4.3	Clocking and Readout	31
5	Setups and Analysis	33
5.1	Setups	33
5.1.1	Motherboard PCB and Insert PCB	33
5.1.2	Data Acquisition system	34
5.1.3	Reference Time Measurement	35
5.1.4	Single Setup	36
5.1.5	Telescope Setup	36
5.2	Analysis	38
5.2.1	Efficiency and Noise	38
5.2.2	Time Resolution	39

5.2.3	Delay Correction	40
5.2.4	Run Correction	41
5.2.5	Time over Threshold	42
5.2.6	Time Walk Correction	43
6	Testbeam at DESY	45
6.1	Noise Structure and Minimum Threshold	46
6.2	Testbeam Results	48
6.2.1	Reference Measurement	48
6.2.2	Time Resolution	49
6.2.3	Time Resolution for Single Pixels	50
7	Single Setup Measurement	53
7.1	High Voltage	54
7.2	VGatePix	55
7.3	VMinusPix	56
7.4	VNFollPix	58
7.5	VPLoadPix	59
7.6	VNPix	61
7.7	VNCompPix	62
7.8	VNFBPix	64
7.9	VPBiasRec and VNBiasRec	65
8	Testbeam at PSI	67
8.1	Standard Configuration	67
8.2	Leakage Current Instability	68
8.3	DAC Parameter Scanning	69
8.3.1	Reference Measurement	69
8.3.2	VGatePix	70
8.3.3	VMinusPix	71
8.3.4	VNFollPix	72
8.3.5	VPLoadPix	73
8.3.6	VNPix	74
8.3.7	VNCompPix	75
8.3.8	VNFBPix	76
8.4	Time Resolution of the optimized Configuration	77
8.4.1	Time Resolution of the Sensor	78
8.4.2	Time Resolution of Single Pixel	79
9	Summary and Discussion	81
10	Bibliography	85

1 Introduction

The Standard Model of Particle Physics is the basic theory which summarizes the current knowledge of the particles and their interactions, and it has been proven over the years by several experiments. The test of the limits of the Standard Model and the search for Physics beyond it at the LHC requires an increase of the accelerators luminosity (HL-LHC), which in turn requires an upgrade of the detector systems to cope with the increased particle rates and irradiation dose. An example of this is the upgrade of the inner tracking system of the ATLAS experiment. This thesis reports on the ATLASPix3 sensor, an HV-MAPS chip, that was proposed for the outermost layer of the ITk. The main goal of this thesis is the optimization of the sensor settings with respect to an optimal time resolution.

1.1 Motivation

The detector for the ATLAS experiment is designed to reconstruct a wide range of particles produced in high energy collisions at the LHC, extracting essential information such as energy, momentum, direction and particle identity. To perform this complex task, the detector is composed of different subdetectors arranged around the centered collision point, as illustrated in figure 1.1.

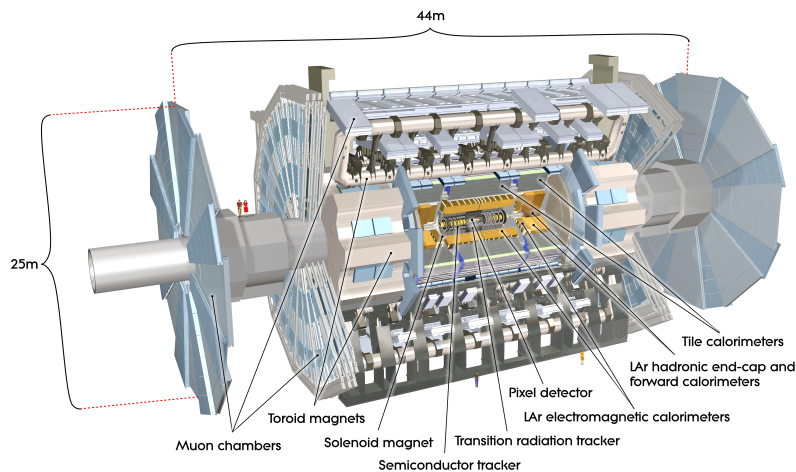


Figure 1.1: Assembly drawing of ATLAS detector. This detector consists of several subdetectors to reconstruct tracks, measure momentum and energy and to identify particles [5].

One of the achievements of ATLAS was the discovery of the Higgs boson in 2012, which allowed to complete the Standard Model of particle physics [3]. However, given its wide range of applications, it is currently used to search for beyond the Standard Model, as well as for precise measurements of the properties of the Standard Model. In the future, the LHC is going to be upgraded to achieve higher luminosities. This upgrade is known as the Phase-2 upgrade or the HL-LHC.

In this phase, the luminosity will be increased roughly by a factor of 5-7. This will have a significant impact on the subdetectors, especially on the pixel detectors, which will have to cope with higher data rates, higher pile-up and higher radiation dose. The requirements of inner tracker is a radiation hardness of 3.8×10^{15} n_{eq}/cm² for the outermost pixel layer and a tracking efficiency of 99% during the time and 97% at the end of the life time of the inner tracker. This efficiency is defined as an In-time efficiency, which requires all hits to be recognized in between two LHC bunch crossings (25 ns). Therefore, a time resolution σ_{time} better than 5 ns has to be achieved for the entire runtime.[4] A new version of the hybrid pixel sensor has been chosen for the HL-LHC upgrade as baseline technology. However, another technology is investigated as an alternative pixel sensor: the High Voltage Monolithic Active Pixel Sensors (HV-MAPS). HV-MAPS uses a commercial CMOS technology in contrast to the hybrid pixel sensors. The advantages of HV-MAPS compared to hybrid pixel sensors are a smaller thickness, which reduces multiple Coulomb scattering. In addition to that, the production costs are significantly lower.[8]

The main goal of this thesis is to present the characterization of ATLASPix3, which is the first full scale prototype of an HV-MAPS, using timing analysis in order to determine a configuration with optimized time resolution, a good efficiency and low noise rate.

1.2 Standard Model

The Standard Model is the theoretical framework of particle physics which explains the fundamental particles and their interactions excluding gravitation. In the Standard Model, three types of particles are described: six quarks and six leptons as fermions and four gauge bosons with spin 1 and the Higgs boson with spin 0.

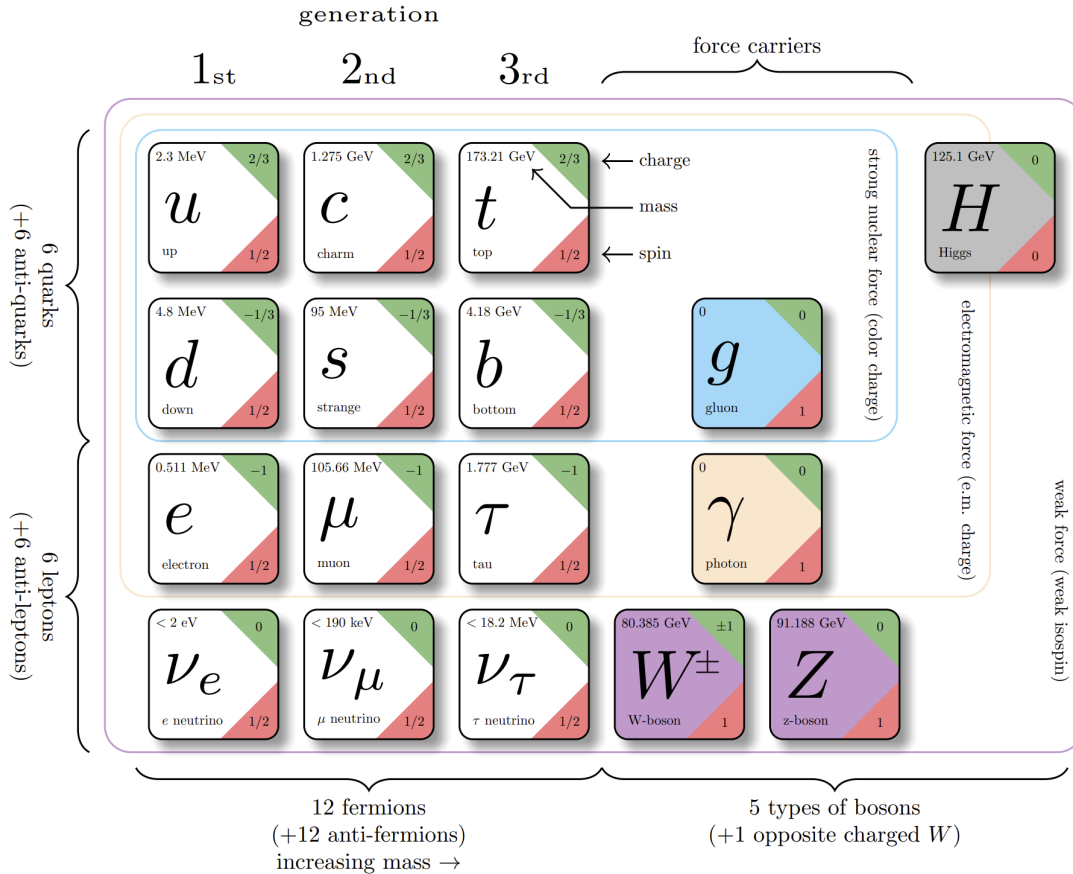


Figure 1.2: The fundamental particles in the Standard Model. [6]

Leptons consist of three generations, electron (e), muon (μ) and tau (τ) with negative charge of -1 as illustrated in Figure 1.2. Each generation features also one neutrino (ν), which is electrically neutral. Neutrinos, which are treated as massless particles in the Standard Model, were proposed by Wolfgang Pauli to ensure conservation of energy explaining missing energy in the β -decay. Neutrinos interact only via the weak force while the charged leptons can interact via the weak and the electromagnetic force. The weak force is mediated by the charged W ($M_W = 80.385 \text{ GeV}$) and neutral Z boson ($M_Z = 91.188 \text{ GeV}$) [6]. For each lepton, there exists an antiparticle. The first observed antiparticle was the positron which has the same mass as the electron but opposite charge. C.D. Anderson, in 1932, observed a

positron using a lead plate in a cloud chamber, which showed bent tracks of charged particles in a magnetic field.[2]

Quarks consist of three generations with two particles each. One series consists of up (u), charm (c), and top (t) with elementary charge $2/3$ while the other series, down (d), strange (s), bottom (b), comes with elementary charge $-1/3$. Quarks can interact via the weak, electromagnetic and strong force. The last one is based on the interaction of the so-called colour charges, which can have three different colours with their corresponding anti-colours. Since a free particle state needs to be colourless, a separation of two or more quarks leads to a production of quark-antiquark pairs. The so created quarks can combine with the initial ones recreating a colourless state. This is called hadronisation or fragmentation. Particles made of more than one quarks are called hadron. A hadron with two quark-antiquark pair is called a meson and with three quarks it is called a baryon. The existence of three types of colours for quarks and gluon was first measured using electron-positron colliding. The annihilation cross section of $(e^-e^+ \rightarrow \mu^+\mu^-)$ was compared to annihilation cross section of jets, which are bunch of produced hadrons by single quarks via hadronization. The result of the measurement matched the calculated branching ratio with the assumption of three colours.

The missing key in the Standard Model was the Higgs boson, which gives mass to the fermions, and the W and Z bosons via spontaneous symmetry breaking. The Higgs boson, with a mass of 125.1 GeV, was discovered at LHC in 2012, using proton collision with a center of mass energy of 8 TeV.[1][3]

Despite the discovery of the missing link Higgs boson, which completed the Standard Model, this theoretical tools can not explain dark matter, gravitation on quantum level, the mass hierarchy of the neutrinos, etc. In addition, the matter-antimatter asymmetry in the universe is not explained sufficiently by the Standard Model. Therefore, experiments like ATLAS can open the possibility to extend this framework or to find new physics beyond the Standard Model.

2 Particle Interaction with Matter

In order to observe particles, they have to interact with the detection medium, which in turn influences the particle itself. In the following, the most relevant types of interactions, for the scope of this thesis, of charged particles with matter are described.

2.1 Charged Particles

In order to understand how charged incident particles lose energy in materials via ionization, the Bethe-Bloch-Formula and Bremsstrahlung are discussed in this chapter.

2.1.1 Heavy Charged Particles

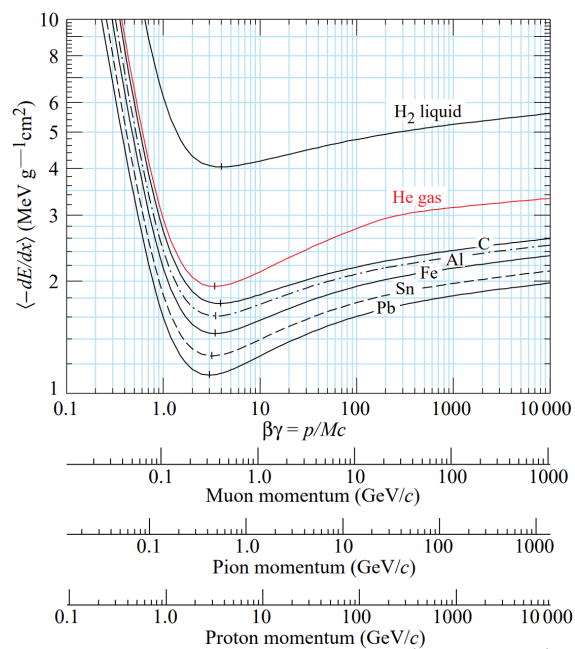


Figure 2.1: Mean energy loss of heavy particles in different materials. For minimum ionizing particles (MIP), $\beta\gamma$ is about 3, for all materials.[6]

When considering interaction with matter, heavy particles are considered as particles with a rest mass larger than $100 \text{ MeV}/c^2$. These particles lose energy mainly via ionization, while traversing a thin layer of material. The quantitative energy loss is

thereby described by a Landau distribution, while the mean energy loss per path length is given by the Bethe-Block formula.

$$-\left\langle \frac{dE}{dx} \right\rangle = \frac{4\pi n z^2}{m_e c^2 \beta^2} \left(\frac{e^2}{4\pi \epsilon_0} \right)^2 \left[\ln \left(\frac{2m_e c^2 \beta^2}{I(I - \beta^2)} \right) - \beta^2 - \frac{\delta(\beta\gamma)}{2} \right] \quad (2.1)$$

The mean energy loss is determined by parameters of the traversing particle as well as the medium: the particle velocity described as $\beta (= \frac{v}{c})$, its charge number z and electron density of the medium n , and the mean of excitation energy I . $\delta(\beta\gamma)$ is the density-effect correction term in the relativistic case. The other parameters are nature constants like the electron mass m_e , the speed of light in vacuum c and the vacuum permittivity ϵ_0 .

Figure 2.2 shows the mean energy loss of heavy charged particles for different materials as predicted by the Bethe-Bloch-Formula. The ionizing energy strongly depends on the momentum of the incident particle.

At $\beta\gamma \simeq 3$, a global minimal energy loss can be observed, which corresponds to a minimal energy deposition in material. This is of high interest in the study of the efficiency of particle detectors.

Over a $\beta\gamma$ of 3, the mean energy loss increases and the effect of δ -electrons which are high-energetic electrons, become more dominant.[6][7]

2.1.2 Electrons and Positrons

In the case of electron and positron the energy loss in material can be described by the Berger-Seltzer formula:

$$-\left\langle \frac{dE}{dx} \right\rangle = \rho \frac{0.153536}{\beta^2} \frac{Z}{A} \left(B_0(T) - \ln \left(\frac{I}{m_e c^2} \right) - \delta \right) \quad (2.2)$$

It depends on the stopping power $B_0(T)$, the the electron density of the medium ρ and the ratio of protons to nucleons Z/A of the medium. There are two effects which cause a difference of energy loss for electron and positron. First, positrons can be annihilated by electrons present in the material. Secondly, due to the indistinguishability of the electrons the Pauli principle has to be considered.[23] These effects result in a slightly larger energy loss for electrons than for positrons at high energies.

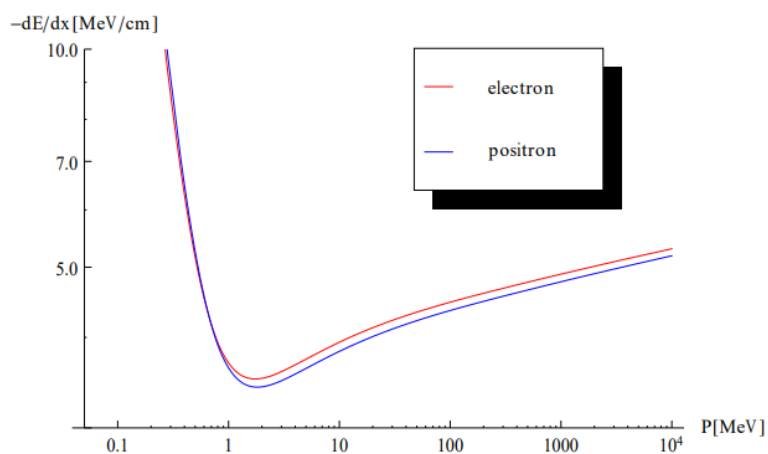


Figure 2.2: Mean energy loss of electrons and positrons in silicon.[23]

2.1.3 Bremsstrahlung

High relativistic particles lose energy in the Coulomb fields of the nuclei in the medium. Electromagnetic interactions decelerate the charged particles while their energy is emitted in form of photons, the so called Bremsstrahlung.

The energy loss for high energetic particles due to the Bremsstrahlung can be described by

$$-\frac{dE}{dx} = \frac{E}{X_0} \quad (2.3)$$

where X_0 is defined as the radiation length which depends on the properties of the material, since X_0 is proportional to the nucleon number A and depends on the charge number Z . [7] This dependency is expressed in the following function:

$$X_0 = \frac{716.4 \text{ g/cm}^2 A}{Z(Z+1)\log(287/\sqrt{Z})} \quad (2.4)$$

2.1.4 Multiple Coulomb Scattering

The incoming charged particle in a medium scatters many times with small angles through the Coulomb fields from nuclei and electrons. The net scattering angle from many small collisions becomes Gaussian via the central limit theorem. The Highland formula describes the angle distribution approximately using Gaussian with RMS width.

$$\Theta_{plane}^{rms} = \frac{13.6 \text{ MeV}}{\beta c p} z \sqrt{\frac{x}{X_0}} \left[1 + 0.038 \ln \left(\frac{x z^2}{X_0 \beta^2} \right) \right] \quad (2.5)$$

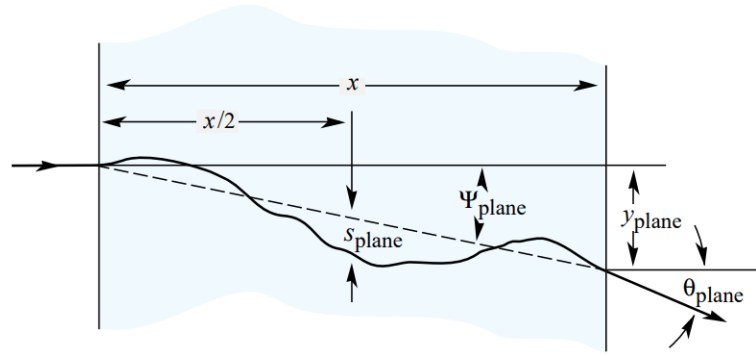


Figure 2.3: The incident particle traveling in the material. [6]

The RMS value of angle is affected by the momentum and velocity of a travelled particle and charge number z . The only parameters which depend on the medium's material are its thickness, x , and X_0 . [6][7]

3 Pixel Detectors

Pixel detectors are devices to detect incident or traversing particles. A typical example of a pixel detector is a digital camera which detects photons and measures their intensities. In this chapter, pixel detectors are described which are designed for the high-energetic particles. In particular, semiconductors like silicon are usable to generate an image of the particles and to build electronics in order to read out data.

The detecting active area is based on a pn-junction (Chapter 3.2) which reduces loss of the generated charges by the interactions of particles with the material. In order to form the pn-junction, doping (Chapter 3.1) is necessary which increases the number of free charge carriers.

Lastly, three different pixel detector types: hybrid pixel detector, monolithic active pixel sensors (MAPS) and high voltage MAPS are introduced in Chapter 3.3.

3.1 Doping

Semiconductors are materials which have a conductivity between conductors and insulators. Intrinsic semiconductors, such as pure silicon and germanium, are not commonly used for electronics applications as their conductivity is too low. In order to increase the number of free charge carriers, impurities are implemented into the atomic lattice. This process is called doping where the doping atoms could be e.g. phosphor, to increase the number of free electron (n-doping) or e.g. boron to increase the number of holes (p-doping). A hole, thereby denotes a free electronic state, which acts as a free positive charge carrier. Due to the increase in the number of free charge carriers, the electrical properties of the semiconductor change, including also its Fermi energy E_F . The Fermi energy at $T=0$ K describes the highest energy state which is occupied by an electron. The Fermi level of intrinsic semiconductors lies around half of the band gap. Using n-doping, the Fermi level is shifted closer to the conduction band while a p-doped semiconductor pushes the Fermi level close to the valence band. This facilitates the thermal creation of free electrons and holes. Their concentration is proportional to the doping concentration.

3.2 PN-Junction

If n- and p-doped materials are brought into contact, a pn-junction or diode is formed. The imbalance of free charge carriers between n- and p-doped material

causes a diffusion current. During this process, electrons and holes recombine in the boundary region of the junction, while the dopant ions remain. This results in space charge regions at the junction, thus a drift current counteracting the diffusion current. An equilibrium state is established in which the boundary region is depleted of free charge carriers, and forms the so-called depletion zone. This zone has a strong electric field acting across it. The according voltage in the depletion zone is described by:

$$V_{bi} = \frac{k_B T}{e} \ln \left(\frac{N_A N_D}{n_i^2} \right) \quad (3.1)$$

where N_A and N_D are the respective doping concentrations and n_i is the intrinsic charge carrier density of the semiconductor.

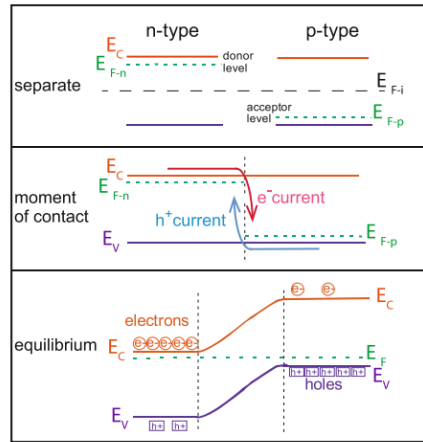


Figure 3.1: Two differently doped semiconductors are brought in contact. Electrons and holes recombine in the boundary region. In equilibrium, an electric field is formed in the depletion zone.[9]

Figure 3.2 shows the difference between forward and reverse biasing of the junction. For forward bias ($V_{ext} > 0$), the depletion zone shrinks since holes are supplied to the p-type and electrons to the n-type region. In contrast, reverse bias extends the depletion zone. The size of the depletion zone with an external voltage V_{ext} applied is described by [9] :

$$w = \sqrt{\frac{2\epsilon_{si}\epsilon_0(V_{bi} - V_{ext})}{e} \frac{N_A + N_D}{N_A N_D}} \quad (3.2)$$

where ϵ_{si} is the dielectric constant.

The current-voltage characteristic is described using an approximation of the Schottky equation [10] as depicted in Figure 3.3. A leakage current is caused by diffusion of free charge carriers from the undepleted volume into the depletion zone and thermal generation of electron-positron pairs in the depletion zone.

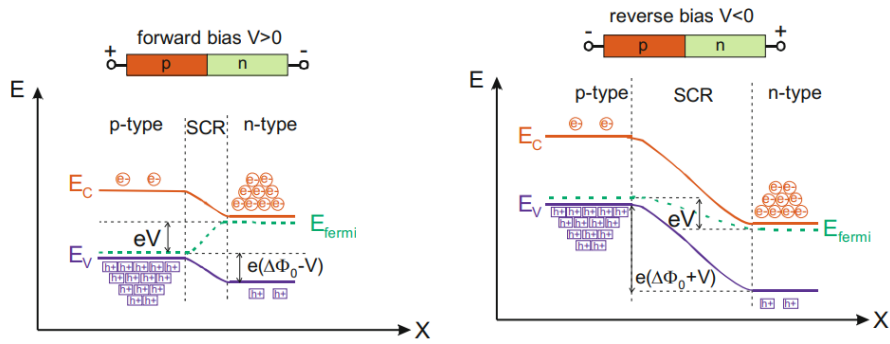


Figure 3.2: The width of the depletion zone depends on the bias voltage. Forward bias shrinks the depletion zone. Reverse bias creates a larger depletion zone.[9]

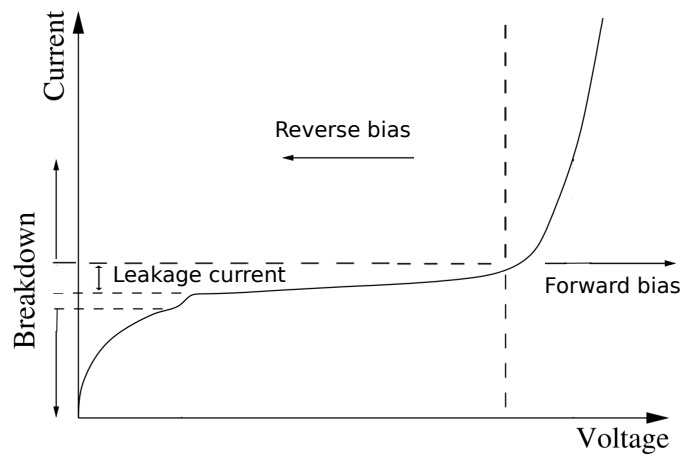


Figure 3.3: The I-V characteristics of the diode. [10]

3.2.1 Signal Generation

Incident particles create free electron-hole pairs in the semiconductor material via ionization. The charge carriers would normally recombine with other free charge carriers in the material or themselves after a certain time. However, if they are created in the depletion zone, there are no free charge carriers to recombine with and the pairs are separated by an electric field. Hence, they travel through the depletion zone via drift until they are collected at the respective electrodes. In case a reverse bias voltage is applied, the signal charges in the depletion zone are collected fast via drift due to the strong electric field. [9]

3.3 Pixel Detectors

In the following, three different types of pixel sensors are introduced and compared with each other: Hybrid Pixel Sensors, Monolithic Active Pixel Sensors (MAPS) and High Voltage MAPS.

3.3.1 Hybrid Pixel Detectors

Hybrid pixel sensors represent a well-established technology in high energy physics experiments. One of the characteristics of hybrid pixel detector is the separation of the readout and the active pixel matrix in two parts. These two chips are connected by bump bonds, as shown in Figure 3.4. For the sensor diode, a high voltage is applied to the substrate to extend the depletion zone and for fast charge collection. Due to separation into two chips, the readout chip is protected to the high voltage. While they reach a high performance standard, the production cost of hybrid pixel sensors is high. In addition, as two separated chips are used, hybrid sensors have a high material budget.

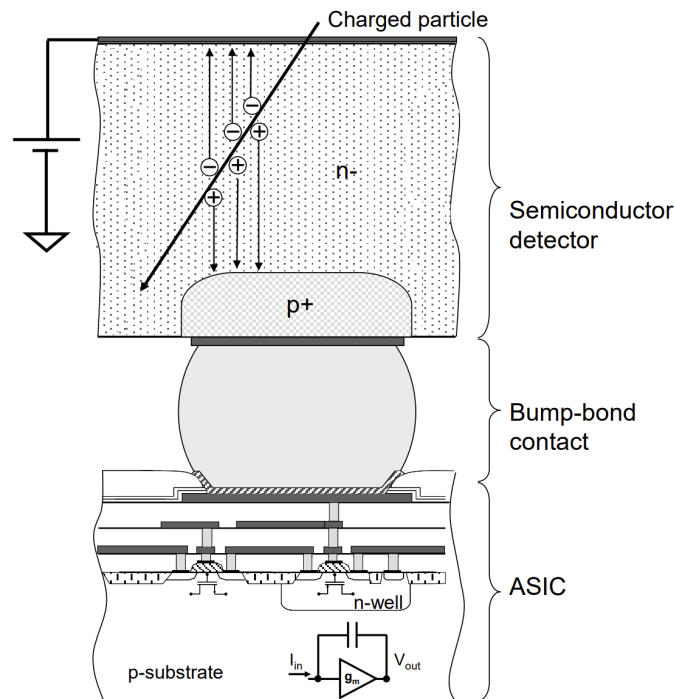


Figure 3.4: Schematic of a hybrid pixel detector. [24]

3.3.2 Monolithic Active Pixel Sensors (MAPS)

In contrast to hybrid pixel sensors, the Monolithic Active Pixel Sensors (MAPS) integrate the readout ASIC and the active detection matrix in one entity. Here, the used commercial CMOS processes reduces the production cost.

One example for a MAPS is the ALPIDE pixel sensor which is developed for the ALICE experiment. Since the charge collection is realized via diffusion, time resolution is limited to a microsecond range.[12]

3.3.3 High Voltage MAPS (HV-MAPS)

Similar to MAPS, HV-MAPS integrates the full readout and the sensor element in one piece of silicon, resulting in a reducible material budget. Furthermore, HV-MAPS can be produced using standard HV-CMOS processes, keeping the production cost lower compared to the hybrid pixel sensor. The sensor diode is reverse biased with a high voltage in order to allow fast charge collection via drift.[12]

The sensor diode is formed by a deep n-well which is implemented in the p-substrate. The HV-CMOS process allows to implement electronics inside the diode's deep n-well, so called floating logic in shallow wells. [21].

The HV-MAPS prototypes were produced for the Mu3e experiment, which searches for charged lepton flavour violating process $\mu \rightarrow eee$ [22].

4 ATLASPix3

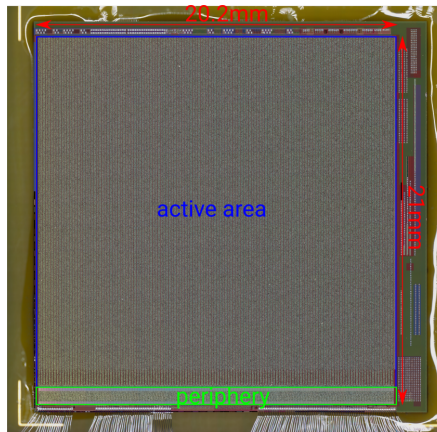


Figure 4.1: Photo of an ATLASPix3 after wire bounding on the insert PCB

ATLASPix3 is the first full-size HV-MAPS prototype with a pixel size of $150\ \mu\text{m} \times 50\ \mu\text{m}$. ATLASPix3 has been implemented in an 180 nm HV-CMOS technology by TSI on wafers with a substrate resistivity of $200\ \Omega\ \text{cm}$. The matrix consists of 132 columns and 372 rows. The total active area can be calculated by the pixel size and the active area of the pixel matrix

$$A_{\text{active}} = (132 \times 372) \times (150\ \mu\text{m} \times 50\ \mu\text{m}) \simeq 3.68\ \text{cm}^2$$

The wafers of ATLASPix3 have been thinned to $100\ \mu\text{m}$. Each pixel is connected point-to-point to its own partner cell in the periphery.

Collected charges in the depletion zone or injected test-pulses are amplified in the pixel by a charge sensitive amplifier (CSA). An in-pixel comparator compares the amplified signal to a threshold level. The discriminated pulse is sent to a partner cell in the periphery by a line driver. In the periphery, a fully integrated state machine steers the conversion of the hit information into digital pixel addresses and timestamps, followed by 8bit/10bit encoding and serialization. The data is sent out zero-suppressed via a Low-Voltage Differential Signaling (LVDS) link at a speed of 1.25 Gb/s.

Threshold and baseline are controlled by voltage digital-to-analog converters (VDACs). The special character of ATLASPix series is that the CSA and the comparator are implemented in the pixel cells. The ATLASPix3 features a purely NMOS-based in-pixel comparator.[13]

4.1 Pixel Cell

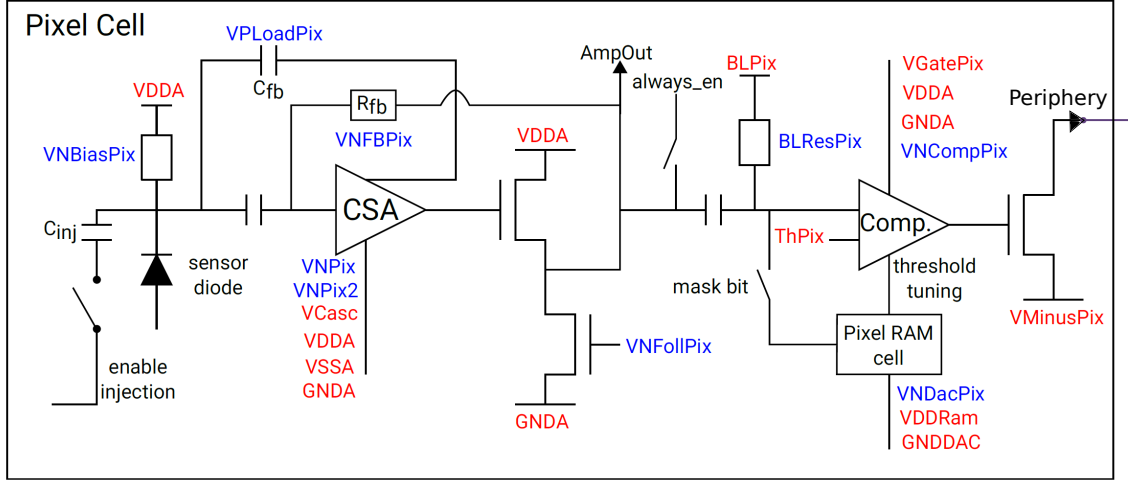


Figure 4.2: Schematic of the ATLASPix3 electronics of a pixel cell with bias voltages.

Charges generated in the diode are collected by the CSA on the feedback capacity C_{fb} , which generates a proportional amplified signal. The capacity is discharged linearly by the feedback circuit R_{fb} , which determines the slope of the falling edge and thereby creates a linear dependence of pulse height and the length. For test purposes a charge signal can be created using a so-called injection coupling AC in to the pixel diode. There is a signal output after the amplification, it is called AmpOut, which can be used to test the CSA. The test output after the CSA called AmpOut requires an additional source follower which is controlled via the DAC VPfollPix.

The DC components of the amplified signals are removed by the AC coupling to the baseline, whose adjustable level is BLPix. The baseline restoration (controlled via BLResPix) acts as a high-pass filter. These signals are compared by an NMOS in-pixel comparator to the threshold level that is set by ThPix. Figure 4.3 shows the circuit of the NMOS-based comparator which is designed using a chain of two differential amplifier stages. The NMOS-comparator requires an extra voltage level, VGatePix which limits the current flow and acts as a load.

After processing in the pixel, the signal is driven to the periphery cell. The voltage amplitude of the line signal is defined by the power domain of the digital part (VDD) as high level and VMinusPix as ground level :

$$V_{\text{line_signal}} \simeq VDD - V\text{MinusPix}$$

VMinusPix has to be tuned to the output range of the NMOS-comparator. For small VMinusPix levels large line signal amplitude can result in cross talk between adjacent signal lines, whereas high VMinusPix levels lead to small line signals, which could not be detected by the receiver stage within the digital partner cell.[8]

The bias voltages are described and summarized in Table 4.1.

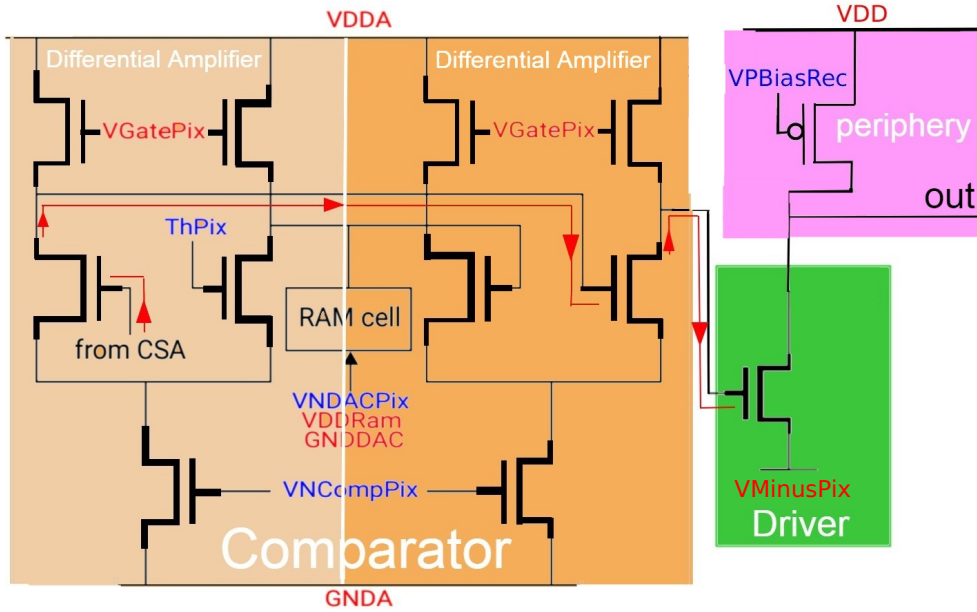


Figure 4.3: Schematic of the NMOS comparator. VGatePix is a necessary part of the NMOS comparator. VMinusPix is the driver to send signals to the peripheral cell. The red line shows the route of the signal in the comparator.

Voltage	Source	Function
VNPix	DAC	Main current source for CSA
VPLoadPix	DAC	Feedback capacitor and amplifier load
VNFBPix	DAC	Resistive feedback
VNFollPix	DAC	Feedback stabilization by source follower
VPFollPix	DAC	Controlling the AmpOut signal
VCasc	Fixed	Amplifier cascade voltage
BLPix	Internal/External	Reference voltage for baseline
BLResPix	DAC	Resistor of baseline restoration
ThPix	Internal/External	Threshold level of comparator
VGatePix	External	Gate level for NMOS comparator
VNCompPix	DAC	Current source of comparator
VMinuPix	External	Ground level of driver
VDDRAM	External	High level for pixel RAM cells
VNDACPix	Internal/External	Reference voltage for tuning

Table 4.1: Bias voltages of the pixel cell.

4.2 Periphery Cell

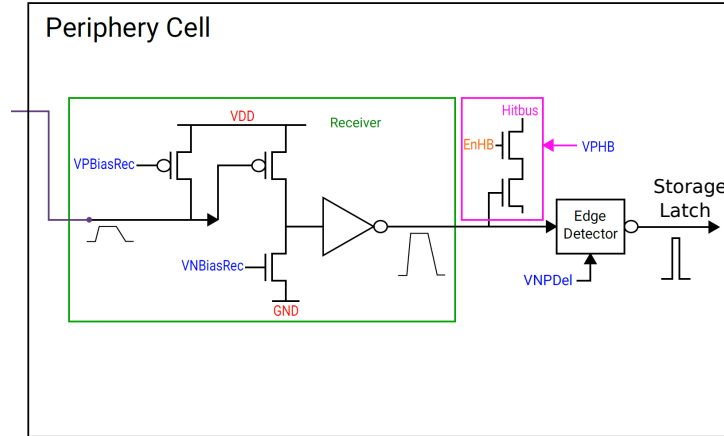


Figure 4.4: Schematic of ATLASPix3 for periphery cell with bias voltages.

After the processing in the pixel cell, the receiver converts the amplitude provided by the line driver. This process is controlled by VNBiasRec and VPBiasRec. In the periphery, the signal is digitized by the edge detector. If a hit is recognized the two time stamps of leading and falling edge of the signal and the column and row addresses are stored.

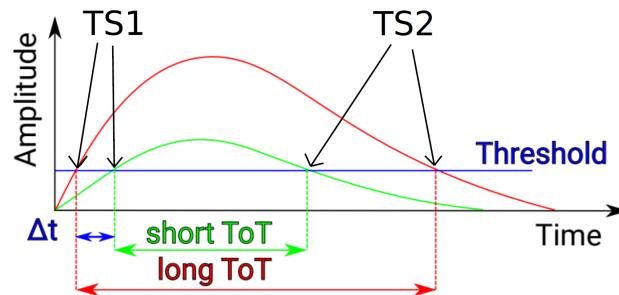


Figure 4.5: The rise of leading edge is stored as timestamp 1 (TS1) and the falling edge of the signal as timestamp 2 (TS2).

The timestamps are generated from the base clock and their sampling speed can be configured via clock dividers (ckdivend and ckdivend2). TS1 (10 bits) is stored when the leading edge of the hit signal crosses the comparator threshold and TS2 (7 bits) when the trailing edge crosses it again (see Figure 4.5). The signal amplitude is directly correlated to the amount of deposited charge in the depletion zone. It causes the sampling latency Δt . To correct this latency, time walk correction is used. More details are explained in Chapter 5.2.6.

Analog to the AmpOut, there is a so-called Hitbus implemented which is a test output of the signal after the receiver stage which is controlled by the DAC VPHB. The Table 4.2 shows the summarized bias voltages of the periphery.

Voltage	Source	Function
VPBiaseRec	DAC	Input level of receiver (PMOS)
VNBiaseRec	DAC	Input level of receiver (NMOS)
VNPEdge	DAC	Current source for edge detector
VPHB	DAC	Hitbus test output controller

Table 4.2: Bias Voltages of the periphery cell

4.3 Clocking and Readout

After sampling in the pixel and periphery cell, the data is readout and serialized by an on-chip state machine and send out as an 8b/10b encoded data stream.

The clocks necessary for this are generated on the chip by a PLL, which locks onto an externally provided reference clock (default 125 MHz). The PLL consists of a phase detector, a charge pump and a VCO. The phase detector compares the clock from the VCO with an externally supplied reference clock and sends a correction signal to the charge pump. The charge pump controlled via VPPump then regulates the VCO, which is controlled by VNVCO and VPVCO. For a reference clock of 125 MHz, the VCO is running at 625 MHz. All subsequent clocks are derived from this clock and can be further modified by clock dividers. A detailed explanation of the PLL is given in [15]. A list of the bias voltages of the PLL is given below in Table 4.3.

Voltage	Source	Function
VPVCO	DAC	Bias current of VCO
VNVCO	DAC	Bias current of VCO
VPPump	DAC	Bias of charge pump
EnPll	DAC	Enables PD

Table 4.3: Bias voltages for PLL

5 Setups and Analysis

This chapter introduces the different measurement setups used in this thesis. In addition, it explains the methods used for analysing the measurement data.

5.1 Setups

There are two different setups used in this thesis, one so-called single setup for laboratory measurements and a telescope setup used at testbeams. Several of their components are common between the two. Those are introduced first.

5.1.1 Motherboard PCB and Insert PCB

The setup used in the context of this thesis to characterize ATLASPix3 is originally developed for characterizing different iterations of the MuPix sensor series. The main test PCB is called motherboard. The sensors are bonded to smaller PCBs with minimum functionality, called inserts, that plug into the motherboard, which provides more flexibility.

The supply voltages for ATLASPix3 (VDD, VDDA, VSSA) are generated by external power supplies and connected to the motherboard. Active components on the motherboard, for example LVDS repeaters, require an additional 5V connection. The test outputs of the sensor (Hitbus and amplifier output) can be probed on the motherboard. Both the motherboard and the insert PCB are shown in figure 5.1.

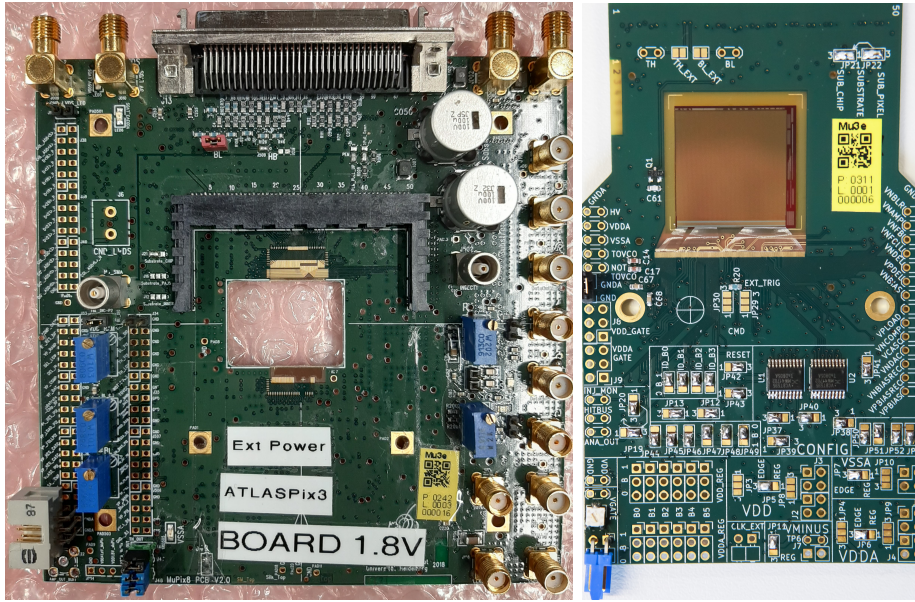


Figure 5.1: (Left) motherboard PCB. (Right) Insert equipped with an ATLASPix3 chip.

5.1.2 Data Acquisition system

The motherboard is connected to a field-programmable gate array (FPGA) via a SCSI-3 cable. The FPGA is used for data acquisition (DAQ) and sensor configuration and it is controlled via a PC through a graphical user interface (GUI). Up to eight MuPix-like sensors, which includes ATLASPix3, can be connected at the same time. Furthermore, there are additional inputs available for example for photomultiplier signals. More detailed information on the DAQ system can be found in [19].

5.1.3 Reference Time Measurement

A scintillating tile, read out by a silicon photomultiplier (SiPM), is used to provide reference time information. The size of the tile is roughly $2\text{ cm} \times 2\text{ cm}$, smaller than the size of ATLASPix3.

The tile and SiPM are covered with an aluminum polyamide laminate to reflect the light on all surfaces. The tile is placed into a 3D-printed frame covered with black tape and black acrylic paint against light from the outside. The tile is mounted to a PCB, which hosts the power connectors for the SiPM, a discriminator, and a LEMO[®] output connector to send the discriminated signal directly to the DAQ system.

A coincidence time resolution of about 2 ns was measured using two tiles.[16] The incoming signal is sampled at 500 MHz by the FPGA resulting in a bin size of 2 ns.

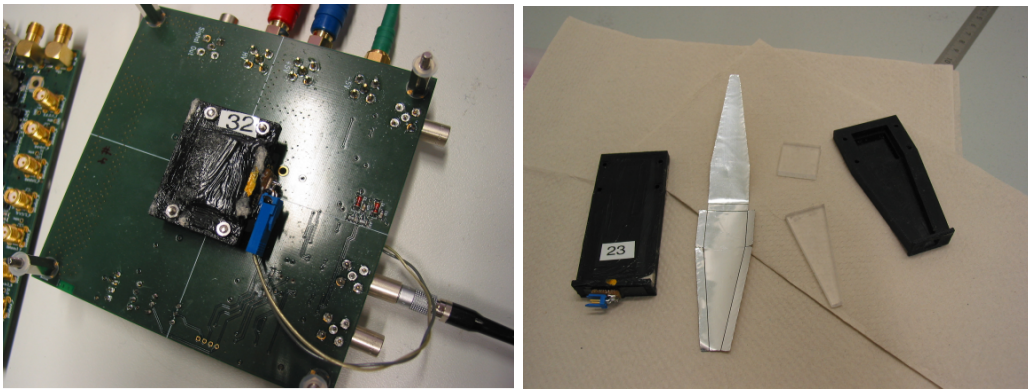


Figure 5.2: (Left) Tile control PCB with tile. (Right) Tile detector [16]

5.1.4 Single Setup

The single setup only uses an ATLASPix3 on an insert connected to a motherboard and optionally a tile as time reference. The amplifier, the digitizing stage, and the data output can be tested using either the injection signal or a radioactive source to characterize the sensor. In the scope of this thesis the single setup is used to optimize the sensor configuration for a good time resolution in the laboratory. A strontium-90 source is placed above the sensor (see Figure 5.3), which provides decay electrons with a spectrum of energies up to ~ 2.2 MeV.

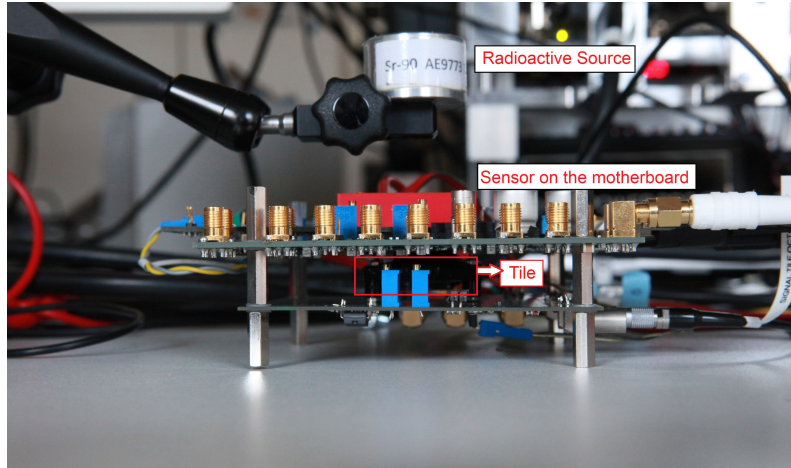


Figure 5.3: Photo of a single setup

5.1.5 Telescope Setup

A beam telescope can be used to measure the efficiency and the noise of a sensor. It consists of several layers of pixel sensors placed consecutively in a particle beam as illustrated in Figure 5.4. A device under test (DUT) is placed inbetween the telescope layers. The position and time of arrival measurements with the telescope layers can be used to reconstruct particle tracks that are compared to hits in the DUT. Details on how efficiency and noise are determined follow in chapter 5.2.1.

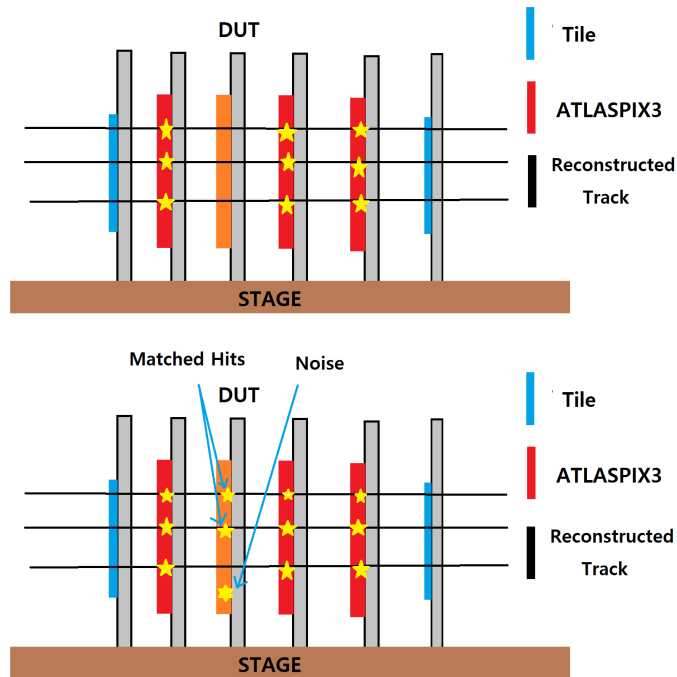


Figure 5.4: A example of the pure ATLASTPix3 telescope. The above figure shows the process of track reconstruction. The below figure shows how to find matched hits and noise.

In the context of this thesis two different sensor types are used as telescope layers. At the testbeam campaign at DESY (see Chapter 6.1) three more ATLASPIX3 sensors are used. At the testbeam campaign at PSI (see Chapter 8.1) three Mupix10 sensors are used instead. MuPix10 is a new full-size HV-MAPS prototype for the Mu3e experiment. The pixel size is $80\ \mu\text{m} \times 80\ \mu\text{m}$ and the size of the sensor is $20.66\ \text{mm} \times 23.13\ \text{mm}$. Its main difference to ATLASPIX3 is that its comparator is implemented in the periphery cell. Also, MuPix10 consists of three pixel matrices, which communicate to the FPGA via different LVDS links [26].

The time resolution of the sensors used as telescope layers is not good enough to measure the time resolution of ATLASPIX3. Therefore, the telescope setup additionally includes two scintillating tile detectors to perform more precise time measurements. At the DESY testbeam the two tiles were placed up and downstream of the telescope. At the PSI testbeam, they were both placed downstream due to the relatively low beam energy, to minimize the effect of multiple scattering on the measurement.

5.2 Analysis

In this section, it is explained how efficiency and noise are determined using measurement data taken with the telescope setup. Furthermore, the timing analysis procedure is outlined. It includes the determination of the time resolution and several offline correction steps.

5.2.1 Efficiency and Noise

The main measurement to judge the performance of a sensor is its hit detection efficiency. The efficiency of a sensor is defined as the ratio between matched tracks and total number of reconstructed tracks in the reference system. For this, the hits in the DUT layer are compared to the acceptable position and timing of the reconstructed tracks.

$$\epsilon = N_{\text{tracks associated with a hit}} / N_{\text{total tracks}} \quad (5.1)$$

The uncertainty on the measured efficiency can be determined using Bayesian statistics. The calculation is implemented in the `TEfficiency` class included in the ROOT libraries [27]. A detailed description can be found in [19].

All non-matched hits on the DUT layer are declared as noise hits in the analysis. The noise rate determined this way does not only contain electronic noise but also additional components stemming from beam particles. Scattering and insufficient focusing of the beam result in some particles not crossing all telescope layers. Furthermore, the usage of a linear fit for track reconstruction disregards tracks with too large scattering angles. Additionally, the telescope layers do have small inefficiencies. Therefore, no absolute statement on the noise rate of the sensor can be made but at least an upper limit can be set. Plus, different sensor configurations can be compared in terms of noise behavior by looking at relative changes in the noise rate.

5.2.2 Time Resolution

The hit timestamp (TS1), which is sampled when the leading edge of the hit signal crosses the comparator threshold level, is compared to reference time information provided by a scintillating tile. The resulting time difference is defined as

$$\text{Time diff.} = \text{TS1} - T_{\text{ref}} \quad (5.2)$$

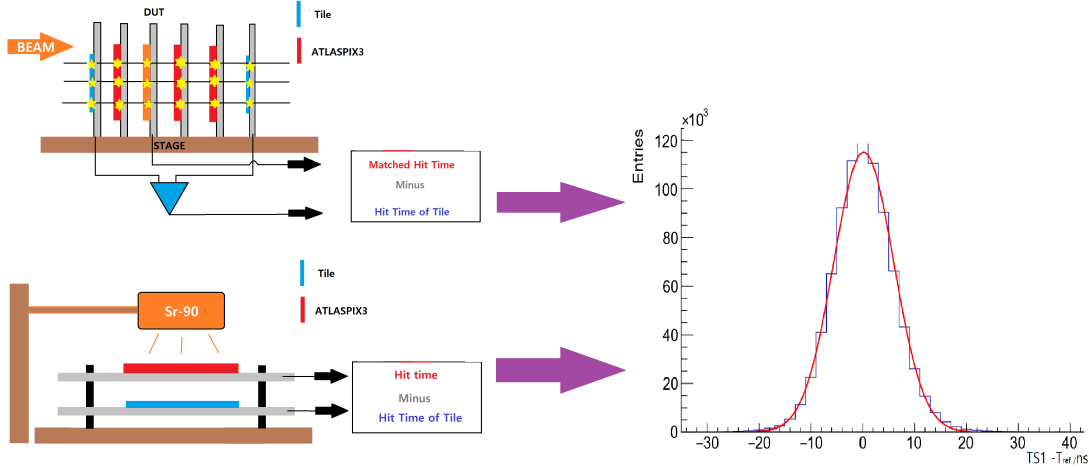


Figure 5.5: Principle how to measure time resolution with the telescope and single setup.

The time difference distribution shows a Gaussian-like shape as shown in Figure 5.6. The single setup cannot distinguish between hit or noise. In this case, the time difference distribution contains noise hits, which broadens the distribution. The time resolution is determined with a Gaussian fit, where the key parameter is the uncertainty sigma σ .

Assuming a box function for the binary time information, the error due to the timestamp binning is given by $\sigma_{bin} = \frac{8 \text{ ns}}{\sqrt{12}}$. Having a bin size of 8 ns the measured time resolution can be corrected offline for the binning contribution as follows:

$$\sigma_{corr} = \sqrt{\sigma^2 - \left(\frac{8 \text{ ns}}{\sqrt{12}}\right)^2} \quad (5.3)$$

5.2.3 Delay Correction

The discriminated signal in the pixel cell is forwarded to its partner cell in the periphery via point-to-point connections. By design, all these metal lines have the same length with small variations in the periphery. This causes delays proportional to these distance variations along the row addresses together with capacitive couplings of the used metal layers. Three metal layers are used for the signal line routing. The small peaks in the delay over row distribution most likely stem from irregular line spacings and the outermost lines on one layer having only one neighboring line.

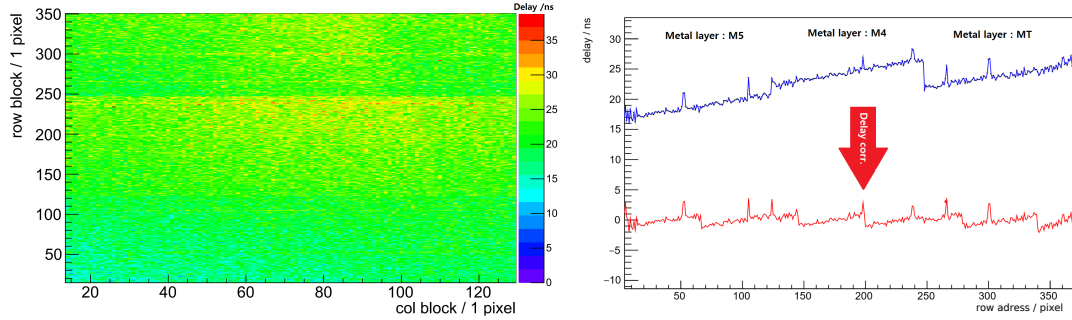


Figure 5.6: Delay map (Left) and delay along the row plot before and after correction (Right) are illustrated.

Since the line delay depends mainly on the row address and for statistical reasons, pixel blocks of 132 columns x 1 row are defined for the delay correction. Due to the three metal layers, three fit functions are used for the delay correction of ATLASPix3:

$$\begin{aligned}
 F_1(x) &= a_1x + b_1 \text{ where } 0 \leq x \leq 124 \\
 F_2(x) &= a_2x + b_2 \text{ where } 125 \leq x \leq 247 \\
 F_3(x) &= a_3x + b_3 \text{ where } 248 \leq x \leq 371
 \end{aligned}$$

where a_i and b_i are fit parameters for i different metal layers. x is the row position of the pixel. Using these parameters, the delay is corrected by

$$\text{Time diff}_{\text{delay_corr}} = \text{TS1} - \text{T}_{\text{ref}} - a_i x - b_i \text{ where } i = 1, 2, 3 \quad (5.4)$$

The structure in the delay over row distribution that remains after the delay correction is assumed to have a negligible effect on the time resolution. The uncertainty σ of the Gaussian fit after this correction is referred to as the delay corrected time resolution.

For the determination of the time resolution of single pixels the above mentioned delay is not of importance. Nevertheless, for further correction steps the individual delay of each pixel is shifted to zero using a Gaussian fit.

5.2.4 Run Correction

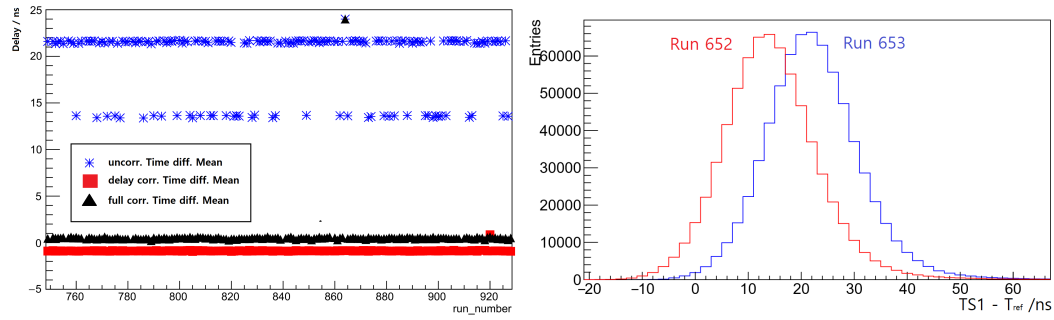


Figure 5.7: Individual run correction.

Typically, the data taken with one sensor configuration is taken in several shorter measurement runs and then combined afterwards into one data set. It is discovered that sometimes the average delay over the full pixel matrix jumps during run change (see figure 5.7). The effect is most likely caused by a resynchronization on reset. It needs to be corrected for before combining data of different runs. Therefore, the delay correction is simply performed for each run separately and the individual distributions are shifted to zero (see figure 5.7). Afterwards, the run data are combined.

5.2.5 Time over Threshold

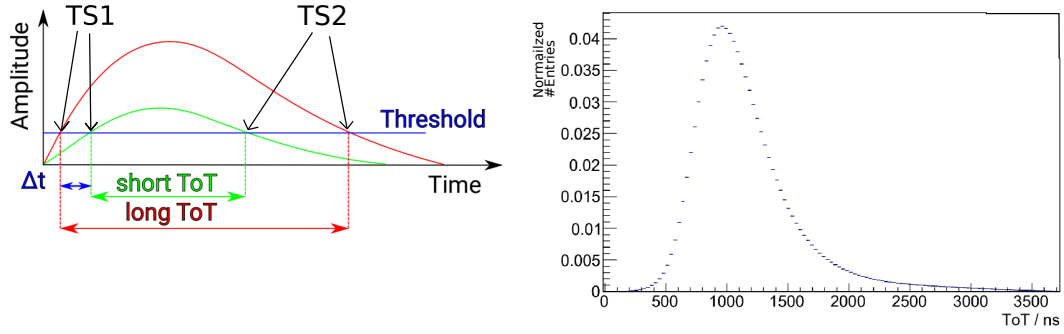


Figure 5.8: Different time over thresholds for different signal amplitudes and a time over threshold distribution for an electron beam.

The time over threshold (ToT) is the time difference between the two crossings of the comparator threshold level by one signal pulse, illustrated in Figure 5.9.

The signal amplitude is directly correlated to the amount of deposited charge of a traversing particle in the detection medium, which can be described by a Landau probability distribution.

In case of ATLASPix3, the times of the two threshold crossings are measured by TS1 (10 bits) and TS2 (7 bits), respectively. The sampling precision of both timestamps can be adjusted via clock dividers called *ckdivend* (TS1) and *ckdivend2* (TS2). *ckdivend* is set to zero to get the highest possible precision on the time of arrival (ToA) of a hit, which is measured by TS1. *ckdivend2* is set large enough so that the ToT spectrum is not cut off at high values. The ToT is then given by:

$$ToT = TS2(1 + ckdivend2) - TS1(1 + ckdivend) \quad (5.5)$$

5.2.6 Time Walk Correction

The ToA sampling time (TS1) is directly correlated to the signal amplitude. For this reason, varying signal amplitudes result in different sampling times of the ToA. This effect is called time walk. By correlating the difference between hit timestamp and reference time information with the ToT information this type of delay can be visualized (see Figure 5.10).

As an offline correction step, weighted maxima of the time difference distributions for small ToT slices (see figure 5.9, top right) are determined and the individual distributions are then shifted such that the maxima coincide with zero. This results in a time walk corrected overall time difference distribution.

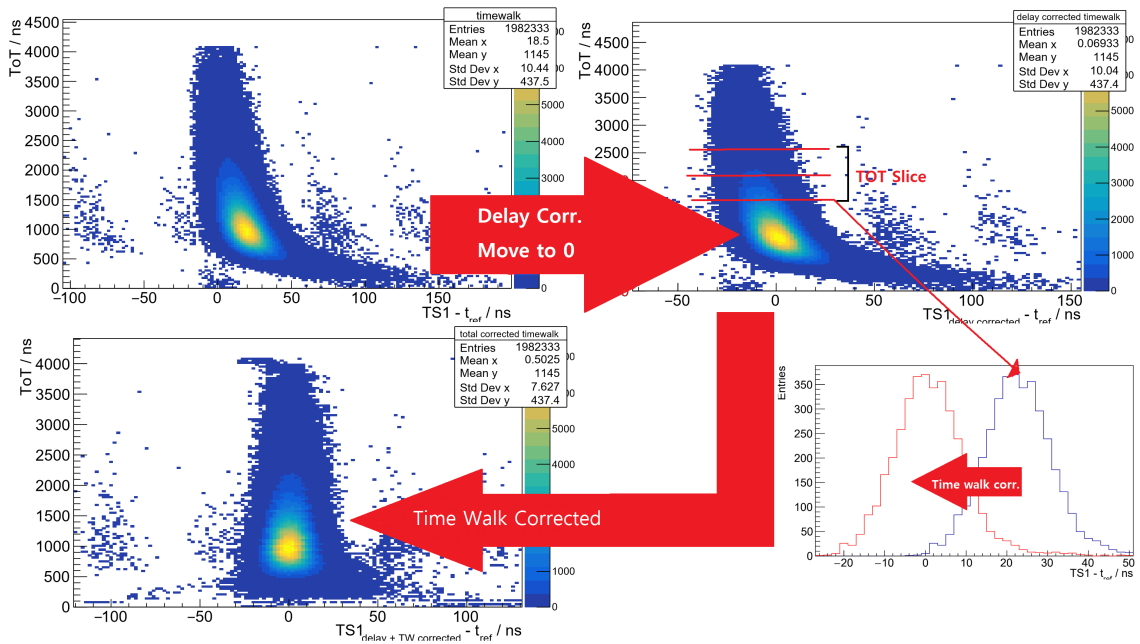


Figure 5.9: Changing of time walk after corrections. After delay correction, ToT slices are moved to nearby 0.

6 Testbeam at DESY

The 'Deutsches Elektronen-Synchrotron' (DESY) is a research center located in Hamburg, Germany. It hosts the DESY II testbeam facility, which provides an electron / positron beam with an energy between 1 GeV and 6 GeV. The beam is created by converting bremsstrahlung photons, created by a carbon fiber target inside the electron synchrotron, into electron-positron pairs via a converter target. The electrons and positrons pass a dipole magnet and a collimator which allow to select the desired particle species and beam energy.

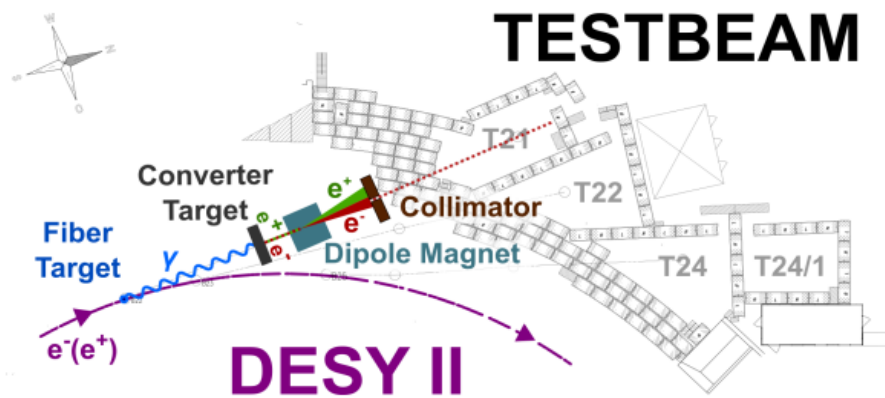


Figure 6.1: Beam line for testbeam at DESY. Electron beam is created with bremsstrahlung photons via interaction with a converter target. [17]

The sensor configuration was optimized during the testbeam for good efficiency and time resolution. For this testbeam, the chosen beam energy is 3 GeV, which allows for a beam rate of 2×10^3 Hz.

6.1 Noise Structure and Minimum Threshold

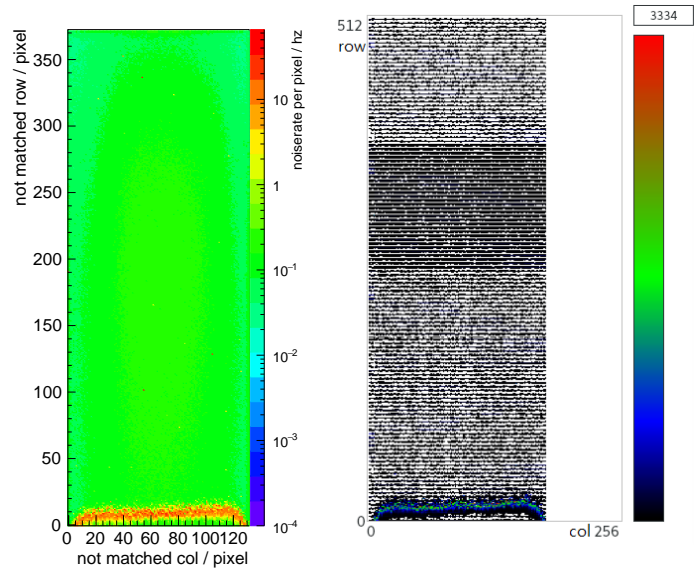


Figure 6.2: Left : a hitmap including intrinsic noise around row address 10.
Right : Noise pattern for a threshold below a critical value.

During sensor commissioning at the testbeam an issue occurred regarding the detection of electronic noise. The issue leads to a specific structure in the hitmap that can be seen in Figure 6.2. In case of the hitmap shown on the left, the comparator threshold was chosen high enough so that the sensor could still be operated with high efficiency. The pattern is caused by the synchronizing reset which is always released before the data sampling. The reset signal has a destructive effect on the stability of the sensor. Therefore, the sensor needs some seconds to stabilize. The hitmap shown on the right is obtained by applying a threshold below a critical value (in the following denoted as minimum threshold) where the sensor performance starts to degrade significantly.

	with bad frames	without bad frames
eff. [%]	99.4	99.8
noise rate[Hz/pixel]	0.9	0.1

Table 6.1: Efficiency and noise rate with and without bad frames.

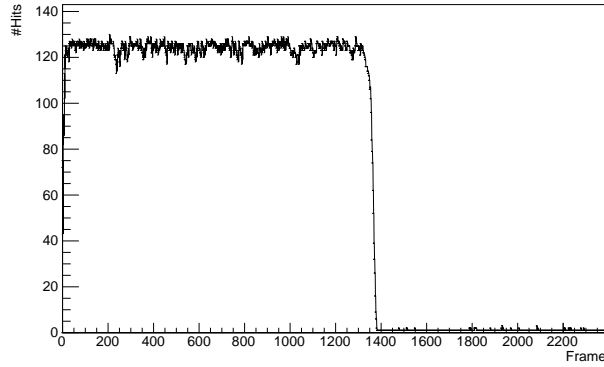


Figure 6.3: Number of hits plotted against frame number.

The noise structure has a negative effect on the results for the measured efficiency and noise rate. Since it is only an artifact of a run start, it was chosen to disregard the according measurement frames in the data analysis as a workaround for this testbeam campaign. Figure 6.3 shows the number of hits per frame. The first 1400 frames are responsible for the noise structure. Table 6.1 shows the results for efficiency and noise rate before and after cutting on those "bad frames". If the data are analyzed without the bad frame cut, the efficiency is 0.4% worse than applying the cut. Also, the noise without the bad frame cut is about 10 times higher, see Figure 6.3. All data are analyzed using this bad frame cut in the following. After the testbeam, this problem is handled by waiting one second after releasing the synchronous reset before starting the data collection.

6.2 Testbeam Results

VNPix [hex]	VNFBPix [hex]	VNCompPix [hex]	VGatePix [V]	VNLoadPix [hex]	VNFollPix [hex]	HV [V]	VMinusPix [mV]	ckdivend2 [hex]
0x10	0x17	0x1f	2.08	0xa	0xa	-60	653	0x3

Table 6.2: Chip configuration used during the testbeam at DESY.

The sensor configuration was optimized for high efficiency and low noise during the testbeam at DESY by systematically varying the settings. The optimized configuration is summarized in Table 6.1.

6.2.1 Reference Measurement

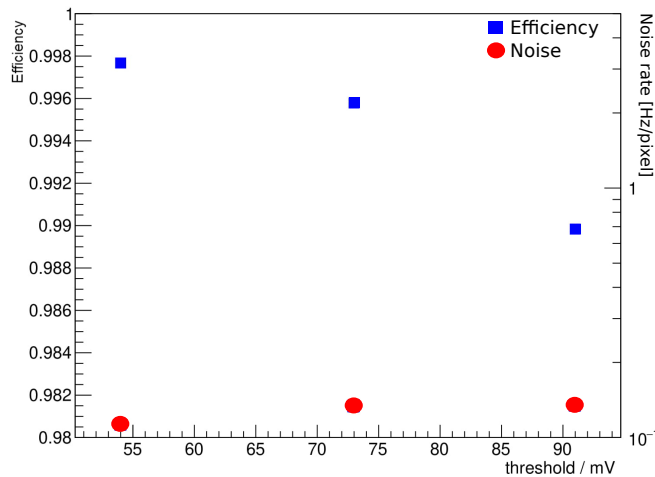


Figure 6.4: Efficiency and noise rate for different threshold levels.

When using the configuration from the Table 6.2 the minimum threshold (see Chapter 6.1) is 54 mV. The efficiency for the minimum threshold is 99.8%. The uncertainty of the efficiency is insignificantly small (about 10^{-3} %). The noise rate for the minimum threshold is still about 0.1 Hz/pixel. The noise structure described in Chapter 6.1 occurs only for the minimum threshold, so there are no bad frames for the thresholds higher than the minimum threshold. The efficiency for the high threshold 91 mV is about 99%. Due to the overall well performance, this configuration is used in order to measure the time resolution.

6.2.2 Time Resolution

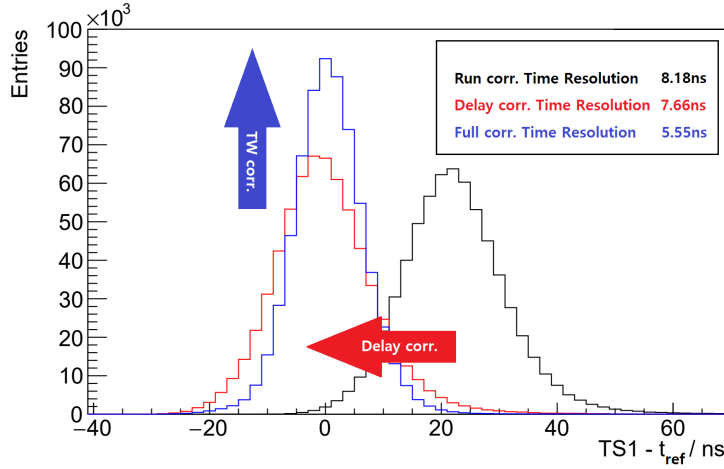


Figure 6.5: Time difference distributions after corrections.

Correction	Time Resolution [ns]	After the binning correction [ns]
Run correction	8.2 ± 0.1	7.9 ± 0.1
delay correction	7.7 ± 0.1	7.3 ± 0.1
Full correction	5.6 ± 0.1	5.0 ± 0.1

Table 6.3: Time resolutions after different corrections. For the binning correction, the bin size for TS1 is 8 ns.

The first result for the time resolution that is presented here is already corrected for varying artificial delays between measurement runs (see Chapter 5.2.5), which stems from an error in the DAQ system, not the sensor.

The errors on the time resolution are determined by comparing the different results one obtains when using different fit ranges. After delay correction (See Chapter 5.2.6) the time resolution improves by 0.5 ns (see Table 6.2). Applying time walk correction further improves the time resolution by additional 2 ns. Subtracting the binning contribution (see Chapter 5.2.3) from the fully corrected result yields a time resolution of (5.0 ± 0.1) ns.

6.2.3 Time Resolution for Single Pixels

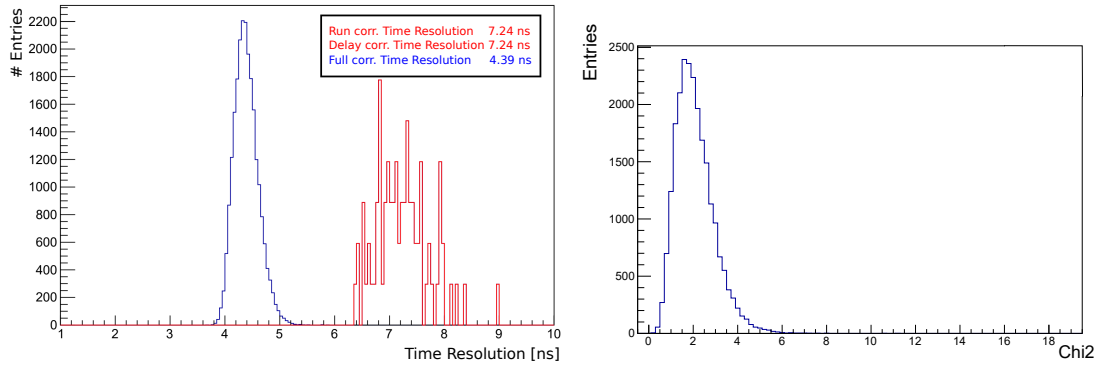


Figure 6.6: Time resolution histograms for single pixel time resolution after different corrections.

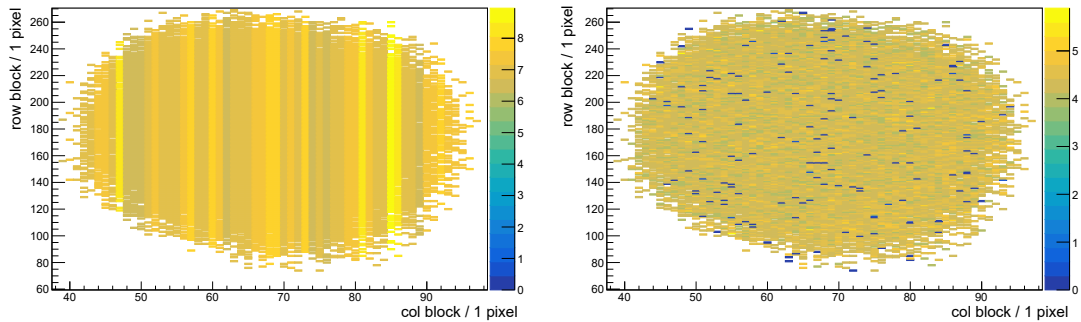


Figure 6.7: Time resolution maps: run and delay corrected (left), full corrected (right). The provided beam at DESY is smaller than the size of the ATLASPix3. Therefore, the region of interest is limited by the number of entries.

Correction	Time Resolution [ns]	After binning correction [ns]
Run correction	7.2 ± 0.6	6.9 ± 0.6
delay correction	7.2 ± 0.6	6.9 ± 0.6
Full correction	4.4 ± 0.2	3.7 ± 0.2

Table 6.4: Mean of time resolution for single pixels after different corrections. For the binning correction, the bin size for TS1 is 8 ns.

A large amount of data has to be collected to be able to study the time resolution of single pixels. The reason for this is statistical, as enough sample size per pixel is required to perform a qualitatively adequate Gaussian fit. Pixels with fewer entries than 3000 were disregarded in the analysis. This applies mostly to pixels close to the sensor edges, since ATLASPix3 has an active area larger than the beam profile at the DESY testbeam. A χ^2 cut of 10 is applied after the fit.

For the time resolution of single pixels the line delay is not of importance. However, for the time walk correction the former steps are necessary and for this reason performed. A mean of the full corrected time resolution of (3.7 ± 0.2) ns is obtained.

7 Single Setup Measurement

The purpose of the single setup in the laboratory is to find a configuration to improve the time resolution with respect to the result from the testbeam at DESY before the testbeam at PSI. Therefore, the most significant DAC parameters are scanned using the single setup and the results are shown in this chapter. The optimal configuration found by analyzing these results is then considered the ATLASPix3 standard configuration.

In this chapter, the results of time resolution and minimum threshold measurement are presented for the parameters shown in Table 4.1, which are important to control the CSA and the comparator. The main current source of the CSA, VNPix, as well as the capacitance and the resistance in the feedback loop affects the shaping of the amplified signals. The performance of the NMOS comparator is determined by VGatePix and VNCompPix. The line driver VMinusPix influences the delay, and it prevents the chip from working if it is set too low or too high. Also the VP- and VNBiasRec DACs are involved in the determination of the delay, in this case on the receiver side. It has to be noted that analog characterization studies have influenced the choice at the following parameter ranges to achieve possible improvements in the time resolution.[25] Since the minimum threshold can be influenced by all the parameters listed in Table 4.1, the minimum threshold is measured for every scan of such parameters. The time difference distributions for the time resolution are fitted with 10 different ranges and the error is computed as the variance of the sigma parameter from the ten fit results.

7.1 High Voltage

VNPix	VNFbPix	VNCompPix	VGatePix [V]	VNLoadPix	VNFollPix	VMinusPix [mV]
16	10	23	2.08	11	7	653

Table 7.1: Measurement configuration for HV.

By applying a reverse bias voltage, one can extend the depletion zone where the generated charges are collected fast via the electric field. The breakdown voltage for ATLASPix3 has been observed at (-64 ± 1) V. Therefore, the measurement range is from -64 V to -5 V with the configuration in Table 7.1.

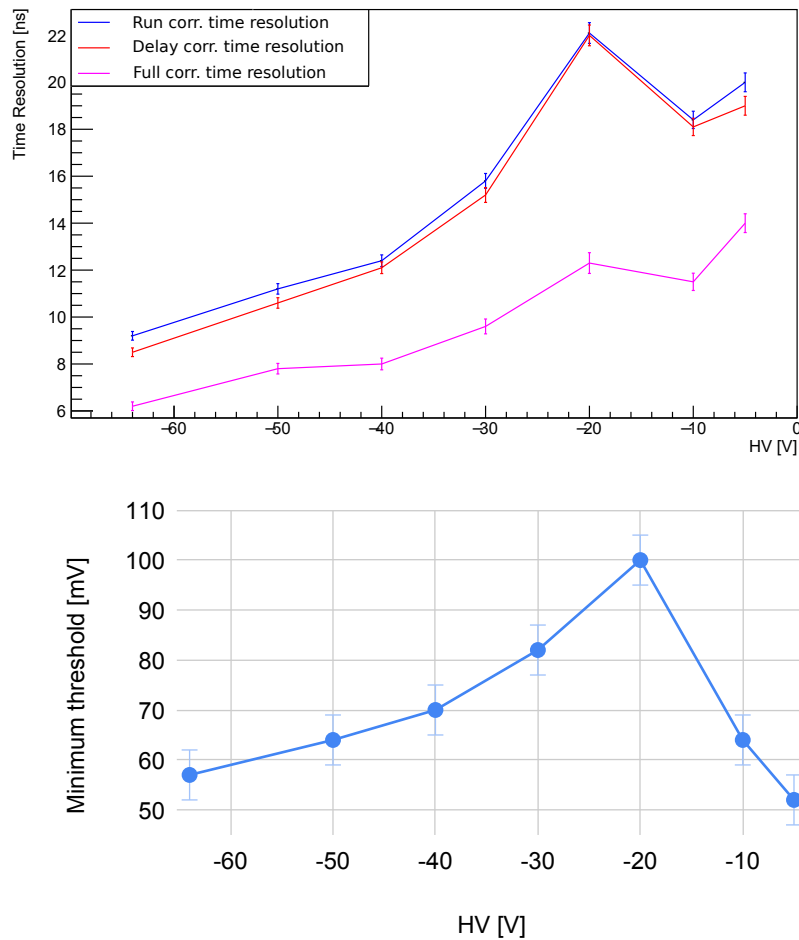


Figure 7.1: Time resolution and minimum threshold for different values of the high voltage.

Both time resolution and minimum threshold follow a similar trend. In the high voltage range from -60 V for -20 V, the time resolution deteriorates as the minimum

threshold level increases, too. The extent of the depletion zone decreases with smaller reverse bias voltage and in the some time the strength of the electric field and thus the speed of the charge collection decreases. The time resolution for the high voltage of -10 V is better than for -20 V . It might be caused by the large difference of the minimum threshold. This instability is unknown.

7.2 VGatePix

VNPix	VNFBPix	VNCompPix	VNLoadPix	VNFollPix	HV [V]	VMinusPix [mV]
16	23	31	10	10	-64	653

Table 7.2: Measurement configuration for VGatePix.

VGatePix is an additionally voltage for the NMOS based comparator, which allows the transistors sets a limit to the current flow in the comparator and act below of the circuit. This voltage level has to exceed VDDA or a permanent current flows in the comparator. VGatePix is powered externally by the motherboard to a maximum of 3.3 V . This voltage is controlled by a potentiometer on the insert. Table 7.2 reports the configuration of all others DACs during the VGatePix scan.

For low VGatePix the minimum threshold level is rather small, and it increases with VGatePix. However, the time resolution has a different trend, see Figure 7.2. VGatePix voltages between 2.02 V and 2.1 V show good performance for the time resolution.

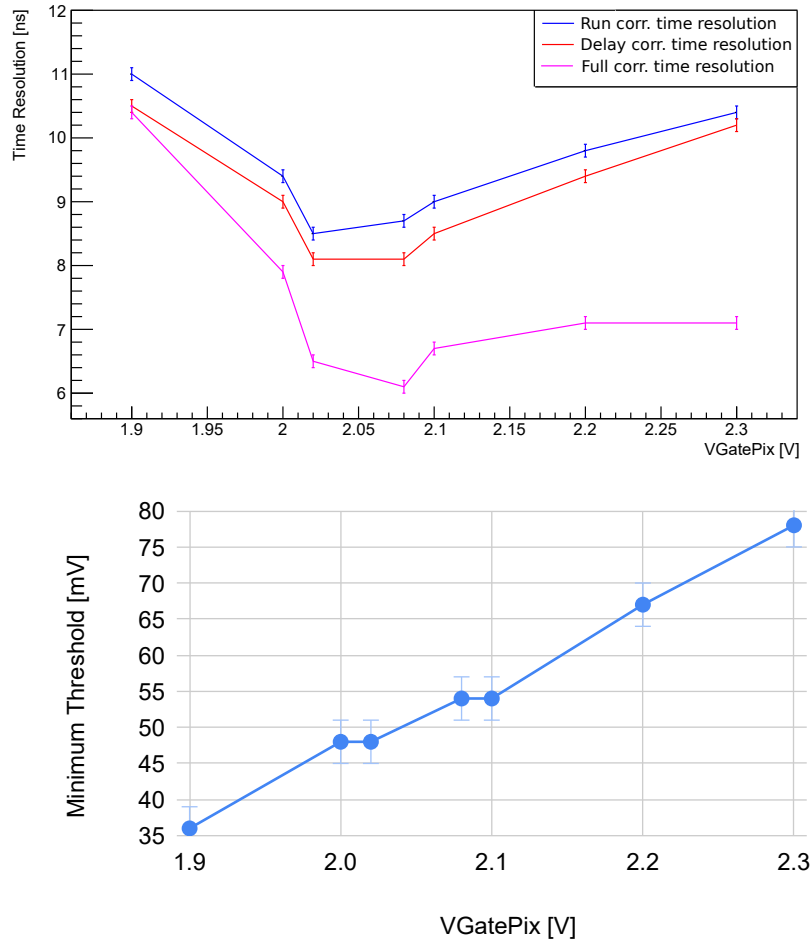


Figure 7.2: Time resolution and minimum threshold for different VGatePix values.

7.3 VMinusPix

VNPix	VNFBPix	VNCompPix	VGatePix [V]	VNLoadPix	VNFollPix	HV [V]
16	23	31	2.08	10	10	-64

Table 7.3: Measurement configuration for VMinusPix.

After being processed in the pixel cells, the signals are driven to the periphery cell. While the high level of the transmission line is given by VDD, its low level is VMinusPix. VDD is powered externally to 1.8 V. VMinusPix can be adjusted in a range between 350 mV and 950 mV, where the lower limit is set by the lower voltage level of the board DAC of the motherboard and the upper limit by the receiver stage in the periphery. To scan VMinusPix, the configuration in Table 7.3 is used.

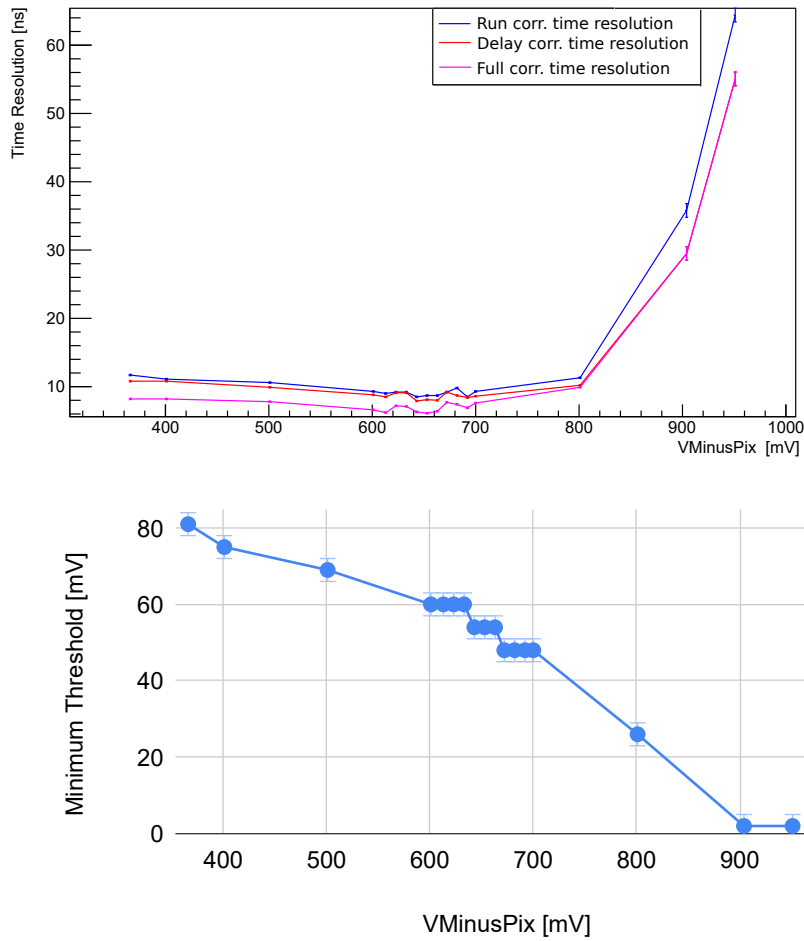


Figure 7.3: Time resolution and minimum threshold for different VMinusPix values.

Figure 7.3 shows that the time resolution, stays stable for VMinusPix lower than 800 mV. The minimum threshold, instead, becomes smaller for larger VMinusPix. However, for VMinusPix larger than 800 mV, the time resolution deteriorates exponentially. Here, the line signal amplitude shrinks to an extend such that it cannot be optimally handled by the receiver stage anymore. The recommended VMinusPix values are therefore between 400 mV and 800 mV.

7.4 VNFollPix

VNPix	VNFbPix	VNCompPix	VGatePix [V]	VNLoadPix	HV [V]	VMinusPix [mV]
16	23	31	2.08	5	-64	653

Table 7.4: Measurement configuration for VNFollPix.

The source follower, which is the internal feedback, stabilizes the amplifier feedback loop. It is already shown in [25] that a certain range for VNFollPix results in high signal amplitudes and short rise time hence, the scan range was chosen to be between 1 and 15 and not the full range.

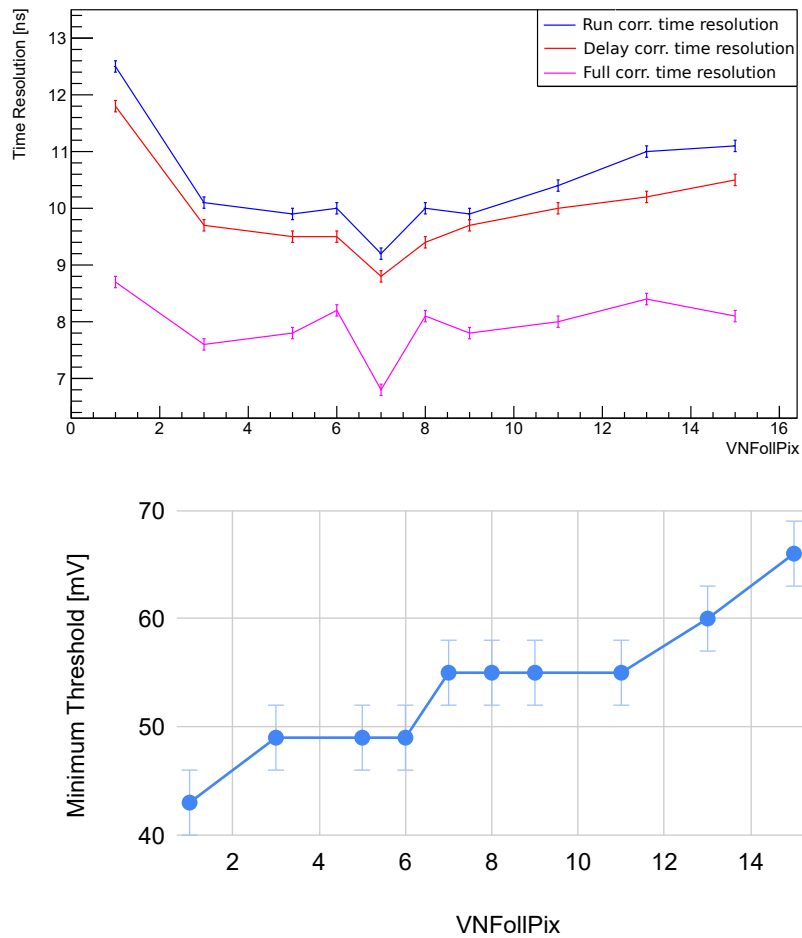


Figure 7.4: Time resolution and minimum threshold for different VNFollPix values.

Figure 7.4 shows that a VNFollPix value of 7 results in the local minima time resolution. The minimum threshold increases with higher VNFollPix values. However, the time resolution does not improve proportional to the threshold level. The reason why VNFollPix 7 is the good value for the time resolutions has to be checked. VNFollPix has, therefore, to be measured in a testbeam campaign.

7.5 VPLoadPix

VNPix	VNFBPix	VNCompPix	VGatePix [V]	VNFollPix	HV [V]	VMinusPix [mV]
16	23	31	2.08	7	-64	653

Table 7.5: Measurement configuration for VNLoadPix.

VPLoadPix controls a the load CSA which also parasitically act as circuit feedback capacitance. From [25] it is known that the signal amplitude decreases with higher values of VPLoadPix. Therefore, a measurement range between 1 and 32 is chosen. The capacitance is not fully charged for a VPLoadPix value lower than 5.[25] The configuration is described in Table 7.5.

The time resolution decreases with higher VPLoadPix until a value of 12, after which it stays stable (Figure 7.5). Since high VPLoadPix values result in an increased power consumption and the time resolution does not significantly improved, an operation range between 7 and 15 is favored. The minimum threshold becomes larger until a VPLoadPix value of 2.

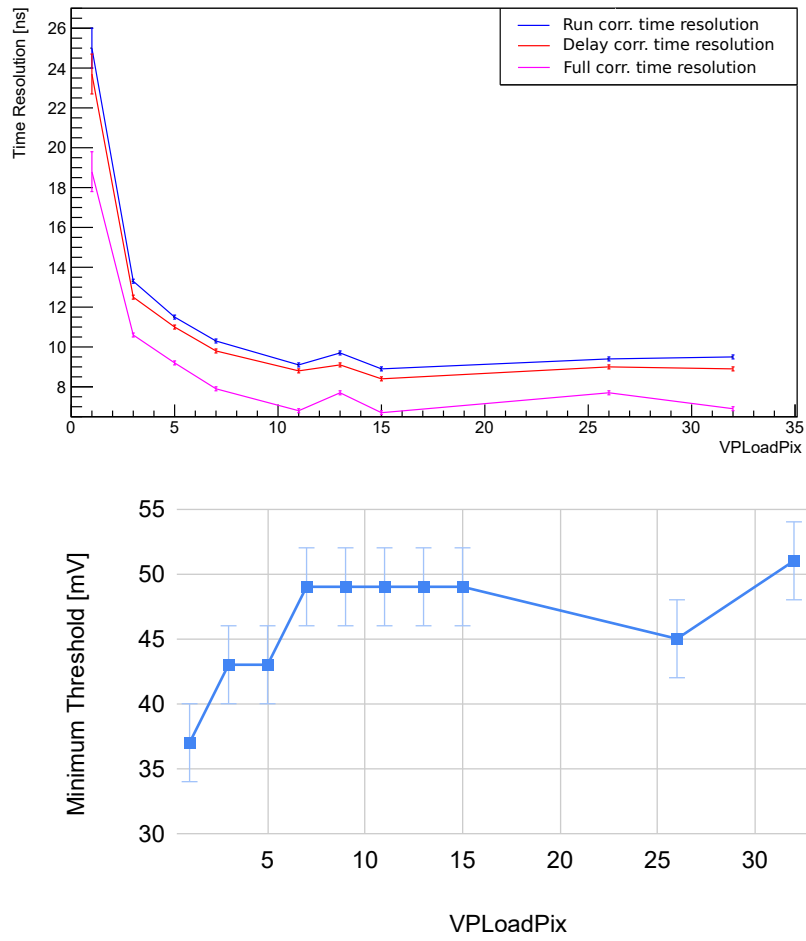


Figure 7.5: Time resolution and minimum threshold for different VPLoadPix values.

7.6 VN Pix

VNFBPix	VNCompPix	VGatePix [V]	VNLoadPix	VNFolPixl	HV [V]	VMinusPix [mV]
20	42	2.08	10	10	-64	653

Table 7.6: Measurement configuration for VN Pix.

VN Pix controls the current flow in the CSA. A stable operation is found to be in the range of 10 to 20. With input from [25] this range was chosen to be investigated for possible improvements of the time resolution. The VN Pix scanning is performed with the configuration in Table 7.6.

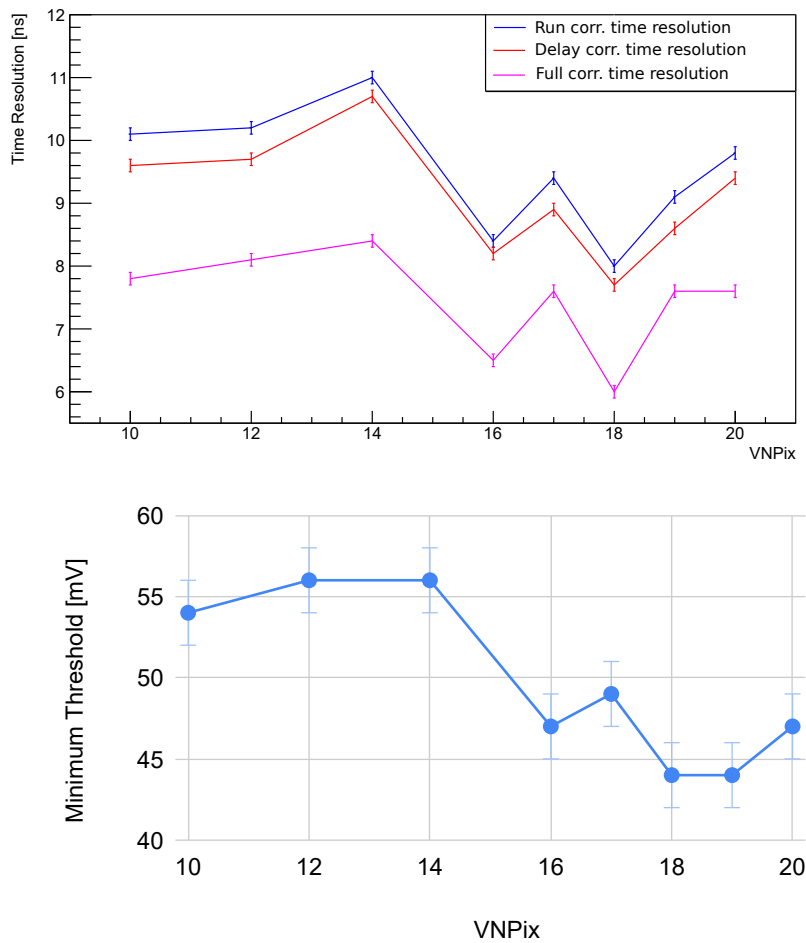


Figure 7.6: Time resolution and minimum threshold for different VN Pix values.

Local minima can be observed between 14 and 20 and therefore this range should be reinvestigated in a testbeam campaign. The minimum threshold decreases with increasing VNPix values. In addition, the time resolution seems to follow the same trend as the minimum threshold.

7.7 VNCompPix

VNPix	VNFBPix	VGatePix [V]	VNLoadPix	VNFollPix	HV [V]	VMinusPix [mV]
16	20	2.08	10	10	-64	653

Table 7.7: Measurement configuration for VNCompPix.

VNCompPix is the main current source of the comparator, and influences significantly the timing performance of the comparator itself. The choice of the measuring range was influenced by a study from [25] which indicates that an investigation of the time resolution in a stable operating range VNCompPix between 10 and 53 can be performed. This measurement is performed with the configuration in Table 7.7.

Figure 7.7, shows local minima in the range between VNCompPix values 15 and 42, while the minimum threshold decreases with increasing values of VNCompPix. In general, large fluctuations can be observed between the measurement points. For further investigation, the above mentioned operating range is of interest.

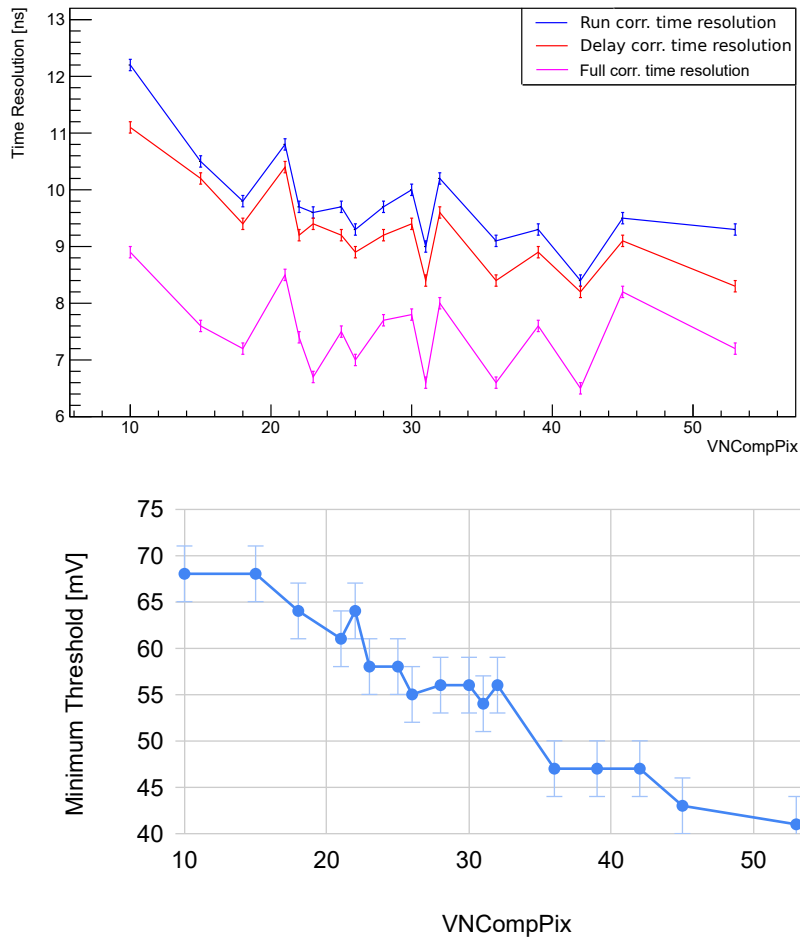


Figure 7.7: Time resolution and minimum threshold for different VNCompPix values.

7.8 VNFBPix

VNPix	VNCompPix	VGatePix	VNLoadPix	VNFollPix	HV [V]	VMinusPix [mV]
16	31	2.08	10	10	-64	653

Table 7.8: Measurement configuration for VNFBPix.

VNFBPix regulates the resistive feedback of the CSA. Previous measurement performed using injection signals show that the amplitude of the output signals decreases significantly with large VNFBPix [25]. Therefore, the scanning range for VNFBPix is chosen between 5 and 45. The Table 7.8 shows the configuration for the VNFBPix scan.

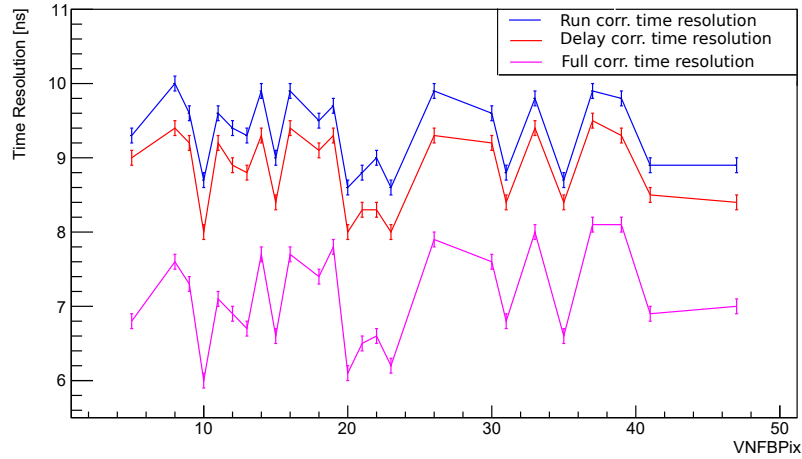


Figure 7.8: Time resolution for different VNFBPix values.

Here, the minimum threshold does not depend on the value of VNFBPix. The time resolution in Figure 7.8 is highly affected by fluctuations, and it is difficult to identify a trend in the plot. Due to the unknown reason of this fluctuation, a conclusive recommendation for a VNFBPix value cannot be given. This measurement should be repeated on a testbeam campaign to connect the achievable time resolution to the efficiency.

7.9 VPBiasRec and VNBiasRec

After being sent through the line driver, the signal is digitized in the periphery. The DAC parameters that influence the time resolution of the receivers are VPBiasRec and VNBiasRec, which control input level of the receiver.

VNPix	VNFBPix	VNCompPix	VGatePix [V]	VNLoadPix	VNFollPix	HV [V]	VMinusPix [mV]
16	10	23	2.08	11	7	-64	653

Table 7.9: Measurement configuration for VN- and VPBiasRec.

Table 7.9 shows the configuration used for the scan of VN- and VPBiasRec. In particular, for the VNBiasRec scan VPBiasRec is set to 30 and vice versa. For both the DACs, the scan range is between 2 and the maximum value 63.

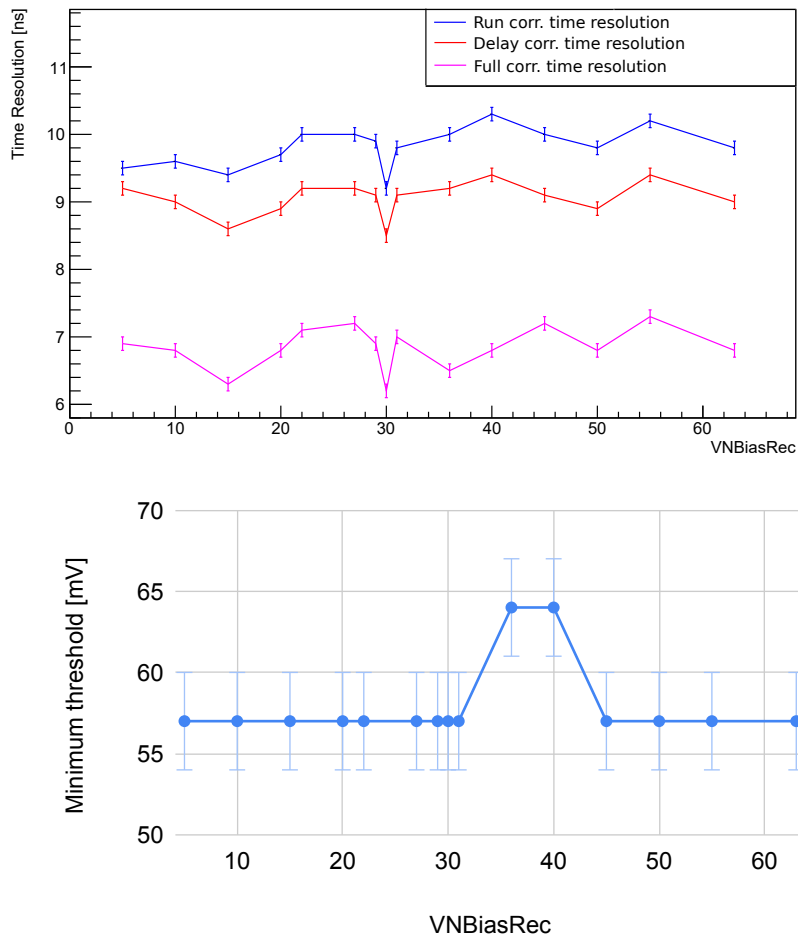


Figure 7.9: Time resolution and minimum threshold for different VNBiasRec values.

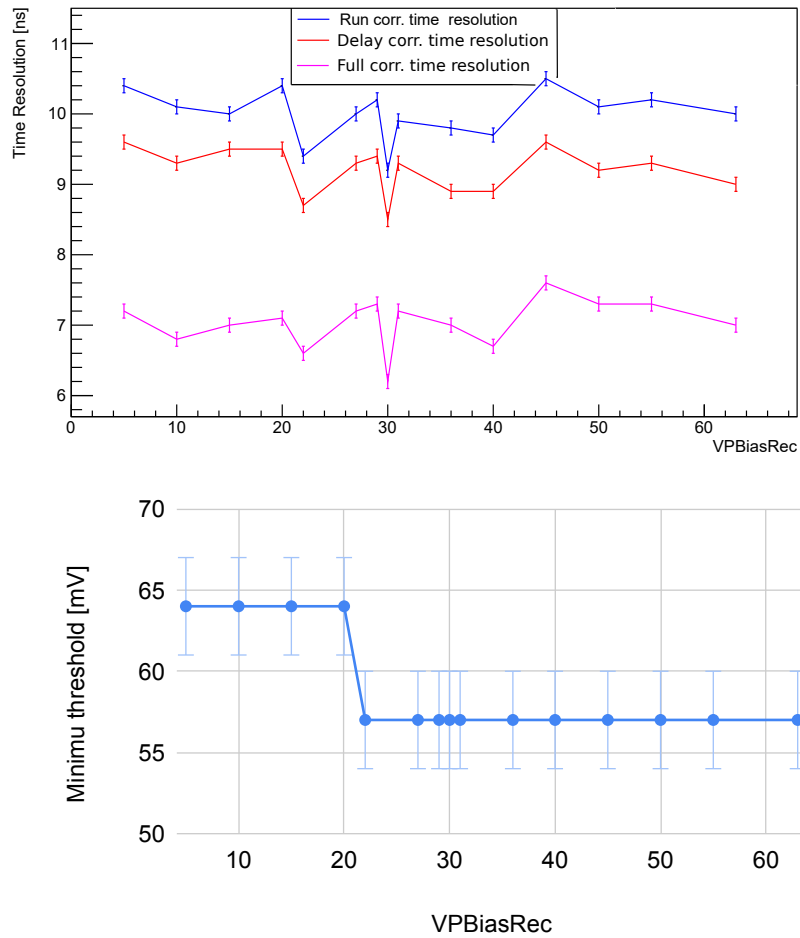


Figure 7.10: Time resolution and minimum threshold for different VPBiasRec values.

The time resolution as a function of VPBiasRec is mostly flat, except for a local minimum at 30. On the other hand, the minimum threshold becomes smaller as VPBiasRec increases. The trend of the time resolution as a function of VNBiasRec is very similar to the one for VPBiasRec with the addition of another minimum at a value of 15. The plot of the minimum threshold as a function of VNBiasRec, instead, shows an increase between 30 and 45, while it stays flat outside that range.

8 Testbeam at PSI

The Paul Scherrer Institut (PSI), located in Villigen, Switzerland, provides a high intensity proton beam at an energy of 590 MeV through its accelerator HIPA.[18] A MuPix10 telescope is installed to characterize ATLASPix3 sensors in the π M1 beam line.

The telescope installed in the π M1 beam line provides a pion beam with a momentum range between 100 and 500 MeV, and a momentum resolution of better than 0.1% can be achieved.[18] The beam momentum is set to 350 MeV with a corresponding beam rate of $8 - 12 \times 10^5$ Hz.

8.1 Standard Configuration

The main goal in this testbeam is to find an optimized configuration for time resolution and to measure the efficiency and noise for different DAC parameters. The studied DACs are related to the analog circuitry, namely the Charge Sensitive Amplifier (CSA), comparator and line driver. Unfortunately, VN-, VPBiasRec could not be measured due to the limited time during the testbeam.

VNPix [hex]	VNFBPix [hex]	VNCompPix [hex]	VGatePix [V]	VNLoadPix [hex]	VNFollPix [hex]	VMinusPix [mV]	ckdivend2 [hex]
0x10	0xa	0x17	2.08	0xb	0x7	653	0x7

Table 8.1: Standard configuration from single setup scanning in the laboratory.

The standard configuration is defined in Table 8.1. Its choice is based on laboratory studies aiming for a good time resolution, as shown in Chapter 7. It is not possible to measure the efficiency and noise in the laboratory, therefore, a detailed look on the individual DAC settings in a testbeam is needed to study also the efficiency and noise behaviours. In addition, the time resolution from the laboratory measurement is not necessarily corresponding to the testbeam one. Since it is not defined for reconstructed tracks, the systematic error in the laboratory is larger than in the testbeam.

8.2 Leakage Current Instability

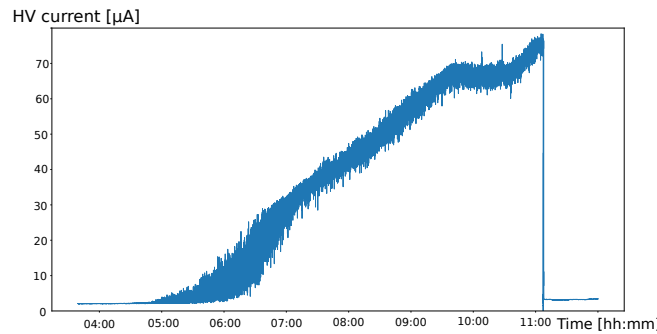


Figure 8.1: A rising high voltage was observed during the testbeam at PSI.

During the DAC scanning, a leakage current instability was observed. Normally, the leakage current is below $10\ \mu\text{A}$ for a high voltage of $-65\ \text{V}$ applied to ATLASPix3. However, since the high rate pion beam might alter the silicon sensor, its current increases (see Figure 8.1). Therefore, the high voltage was decreased to $-60\ \text{V}$ for some DAC parameter scans and the measurement of the time resolution with the optimized configuration.

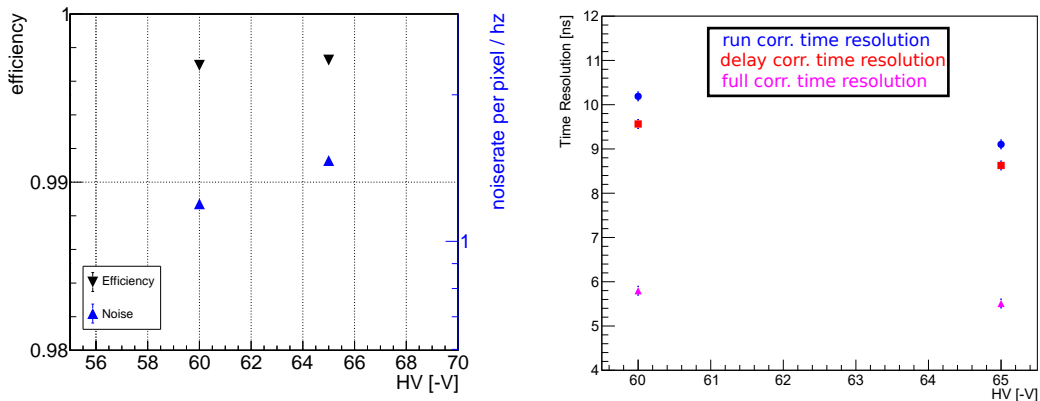


Figure 8.2: Comparing the efficiency and noise and time resolution for $-60\ \text{V}$ to $-65\ \text{V}$

The minimum threshold for a high voltage of $-65\ \text{V}$ is the same as for $-60\ \text{V}$. However, the efficiency, noise rate and time resolution are different. The efficiency is not changed much (see Figure 8.2), but the noise rate for $-65\ \text{V}$ is higher than for $-60\ \text{V}$, since the leakage current of the diode increases. The run and delay corrected time resolution for $-65\ \text{V}$ are about $1\ \text{ns}$ better than for $-60\ \text{V}$. After time walk correction, the difference of time resolution is about $0.4\ \text{ns}$. So, the results of the scans and the time resolution measurement for the optimized configuration using a

high voltage of -60 V has to be viewed considering this effect.

8.3 DAC Parameter Scanning

8.3.1 Reference Measurement

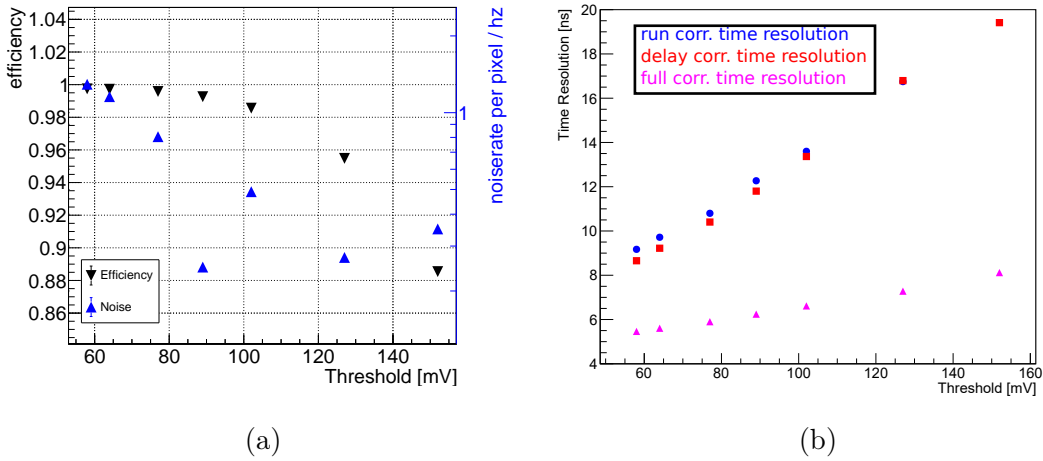


Figure 8.3: (a) Efficiency and noise rate, (b) time resolution for different threshold with an HV of -65 V .

First, the efficiency and noise rate are measured for the standard configuration, i.e. the configuration obtained from the lab tests (see Chapter 7). The error of the efficiency is always quite small (about $10^{-3}\%$) compared to the required sensitivity (only changes on permille level are of interest). The efficiency for a threshold of 56 mV is 99.7% while the noise rate is about 1 Hz/pixel . For a threshold of 100 mV , the noise rate is higher than for threshold 90 mV . This increase at 100 mV can be explained by a change in the beam rate. The noise rate is higher compared to the DESY testbeam, since a different type of telescope is used and multiple scattering is much more dominant at PSI.

The time resolution for the minimum threshold of 56 mV is $(9.0 \pm 0.1)\text{ ns}$ after run correction and $(8.2 \pm 0.1)\text{ ns}$ after delay correction, $(5.4 \pm 0.1)\text{ ns}$ after full correction, but without binning correction. Compared to the result of the DESY testbeam, the run and delay corrected time resolution with the standard configuration is about 0.5 ns worse. The full corrected time resolution is 0.2 ns better. This was achieved by the choice of a larger `ckdivend2` value. The value was set to 7 (3 at DESY) extending the width of the ToT spectrum.

8.3.2 VGatePix

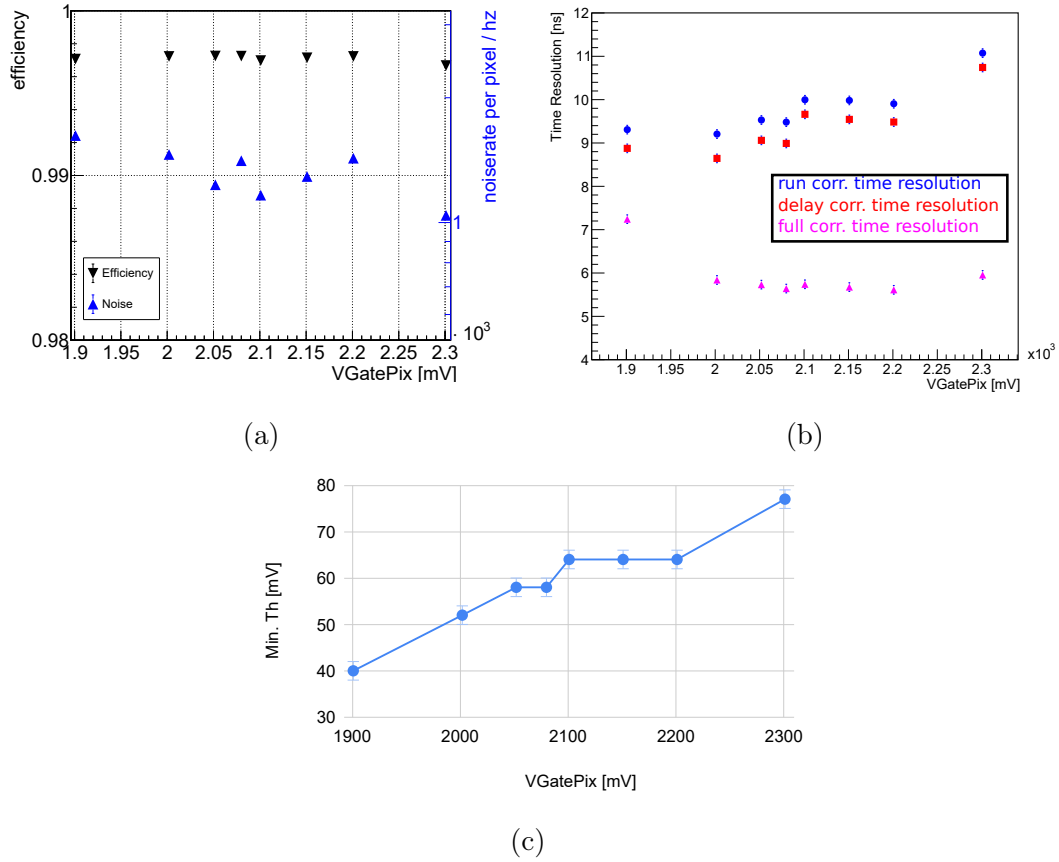


Figure 8.4: (a) Efficiency and noise rate, (b) time resolution, (c) minimum threshold for different VGatePix values with an HV of -60 V.

VGatePix has to be larger than 1.8 V which is the base level. So, VGate is measured between 1.9 V and 2.3 V. The plot (a) in Figure 8.4 shows that the efficiency for all measured VGatePix value is over 99.7% with small error (about 10^{-3} %). The noise rate varies very little for different VGatePix values, from about 1 Hz/pixel to 1.5 Hz/pixel.

The tendency of the minimum threshold is corresponding to the measurement in the laboratory, see Chapter 7.2.1. However, the resulting time resolution is different to the one obtained in the laboratory. Since the time resolution in the testbeam is calculated from timestamps of matched hits to tracks from the telescope, the result of testbeam is more precise than the result in the laboratory. The run and delay corrected time resolution follow the behaviours of the minimum thresholds, except VGate 1.9 V. The full corrected time resolution, however, is stable between 2.0 V and 2.2 V. For the time resolution, VGatePix 2.0 V or 2.08 V is recommended, since the run and delay corrected time resolution is better than the VGatePix value between 2.1 V and 2.2 V.

8.3.3 VMinusPix

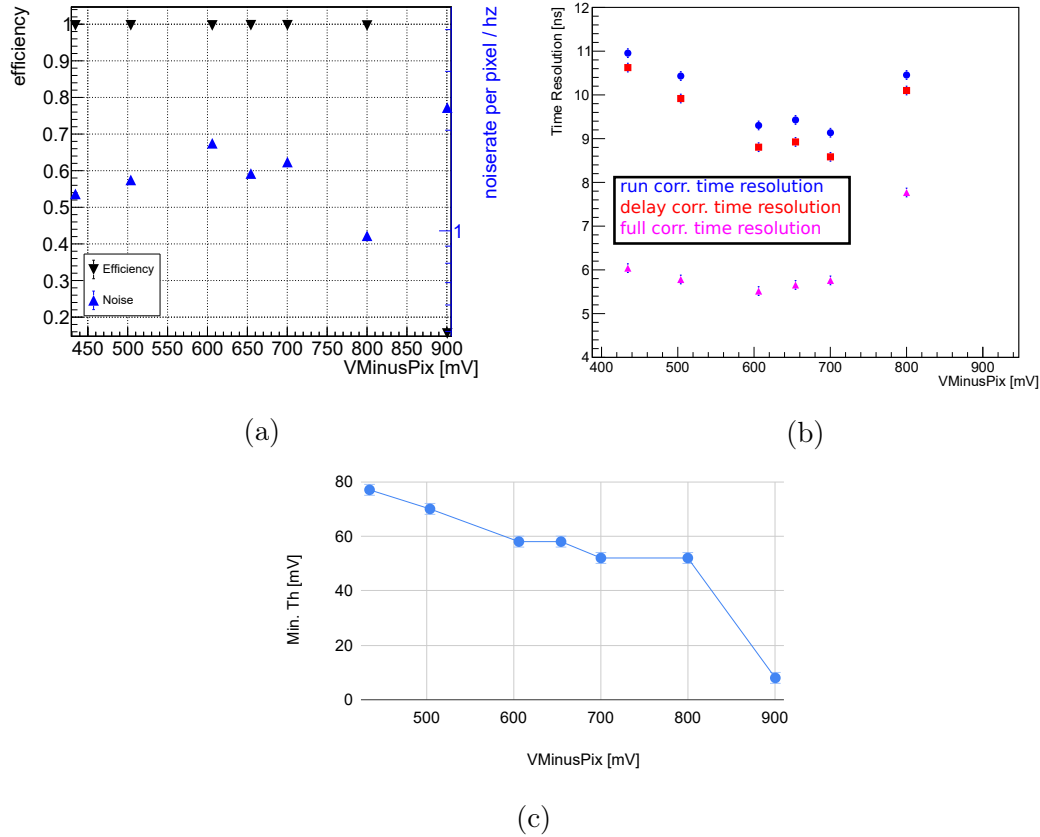


Figure 8.5: (a) Efficiency and noise rate, (b) time resolution, (c) minimum threshold for different VMinusPix values with an HV of -60 V.

VMinusPix which controls the level of the line signals is powered from the motherboard PCB externally. The minimum VMinusPix value is about 350 mV and the maximum is 3.3 V. The optimal range is between 440 and 900 mV. The efficiency drops to $< 20\%$ for VMinusPix values above 900 mV. Therefore, it is not possible to measure time resolutions for such values.

For VMinusPix < 900 mV, the efficiency is about 99.7%. The noise rate for 800 mV is the lowest, but has the worst time resolution.

Between 430 mV and 700 mV, the run corrected and delay corrected time resolution follows the minimum threshold behaviour. Full corrected time resolution, however, increases with higher VMinusPix, but not significantly. Therefore, a VMinusPix value between 600 mV and 700 mV is recommended.

8.3.4 VNFollPix

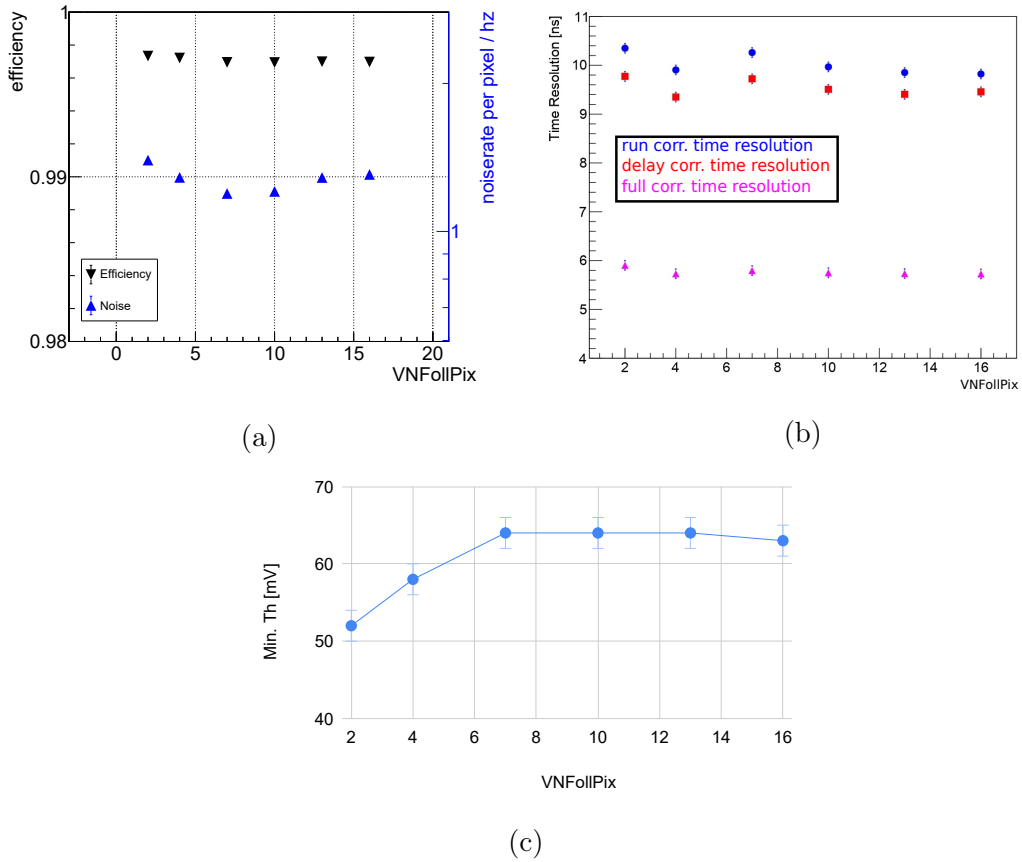


Figure 8.6: (a) Efficiency and noise rate, (b) time resolution, (c) minimum threshold for different VNFollPix values with an HV of -60 V

VNFollPix is measured in the same range as the measurements in the laboratory. The efficiency is not dependent on VNFollPix. The time resolution is almost the same with a slight preference for higher VNFollPix values. The noise rate has a minimum between VNFollPix 5 and 11. Therefore, VNFollPix 7 is recommended due to the low noise rate.

The minimum threshold plot in the laboratory has a different tendency compared to the plot in the testbeam, see Chapter 7.2.3. This might be connected to systematic effects from the different environments.

8.3.5 VPLoadPix

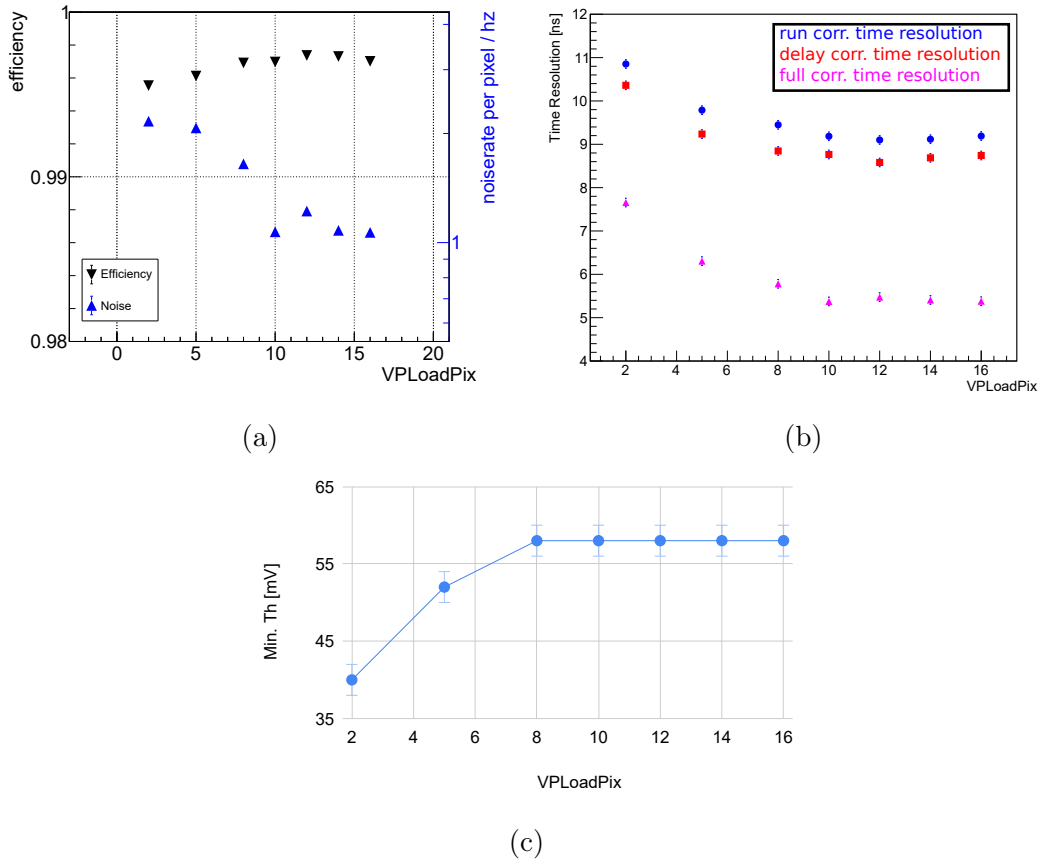


Figure 8.7: (a) Efficiency and noise rate, (b) time resolution, (c) minimum threshold for different VPLoadPix values with an HV of -65 V

The measured range for VPLoadPix is limited from 2 to 16, because it is expected that the time resolution and the minimum threshold are stable for even higher VPLoadPix. The result shows the same behavior as the laboratory measurement, see Chapter 7.2.4.

With VPLoadPix higher than 10, the time resolution is stable. The minimum threshold is stable with values higher than 8. The efficiency for VPLoadPix smaller than 8 is decreases significantly. The noise rate is decreased for high VPLoadPix values. With VPLoadPix higher than 10, the noise rate stabilizes to about 1 Hz/pixel. Therefore, it is recommended to set VPLoadPix to a values higher than 10.

8.3.6 VN Pix

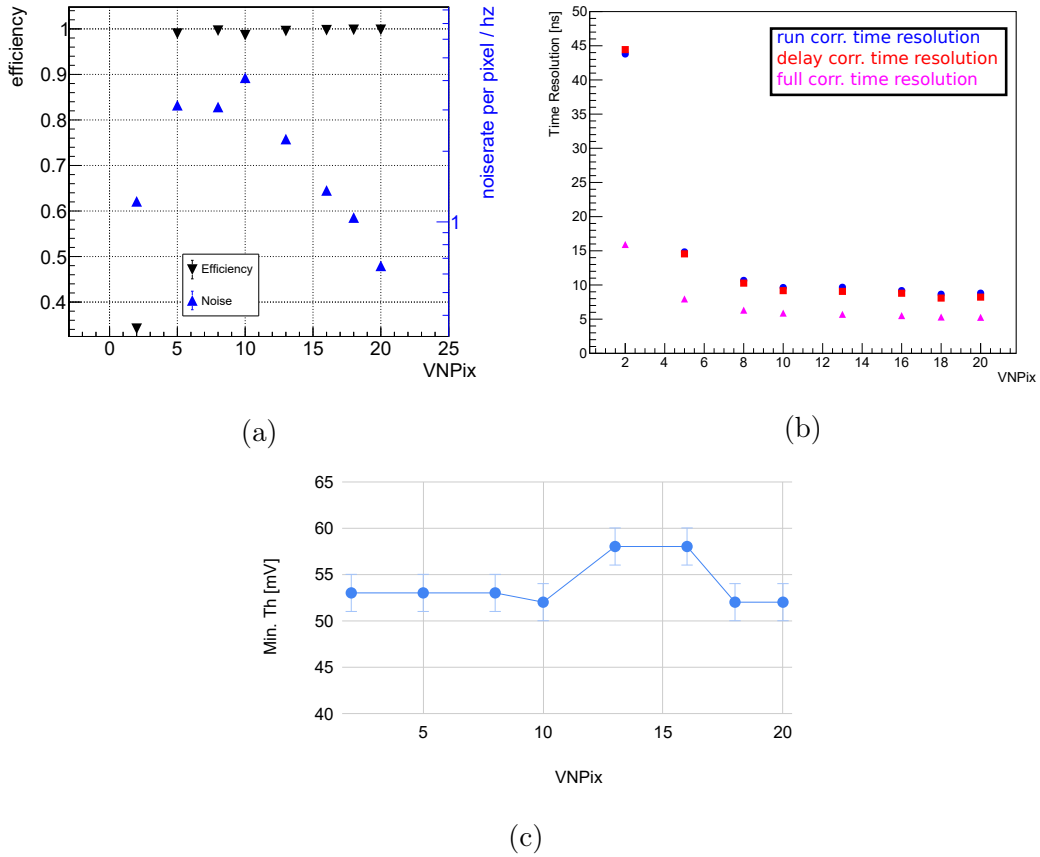


Figure 8.8: (a) Efficiency and noise, (b) time resolution, (c) minimum threshold for different VN Pix values with an HV of -65 V

VN Pix, which is the main current for CSA, is characterized for values between 2 to 20. The studied range is the same as for the measurement in the laboratory. The results for VN Pix in laboratory and testbeam, though, are different. In the laboratory, VN Pix smaller than 10 leads to a non-working configuration. In the testbeam, instead, these values could be operated without any problems. Perhaps, the testbeam setup for VN Pix is more stable than in the laboratory, see Chapter 7.2.5.

The efficiency for VN Pix higher than 5 is 99.7%. The noise rate is decreased for higher VN Pix. The time resolution becomes smaller for higher VN Pix as well. For noise reduction and superior time resolution, a VN Pix value between 10 and 20 is recommended.

8.3.7 VNCompPix

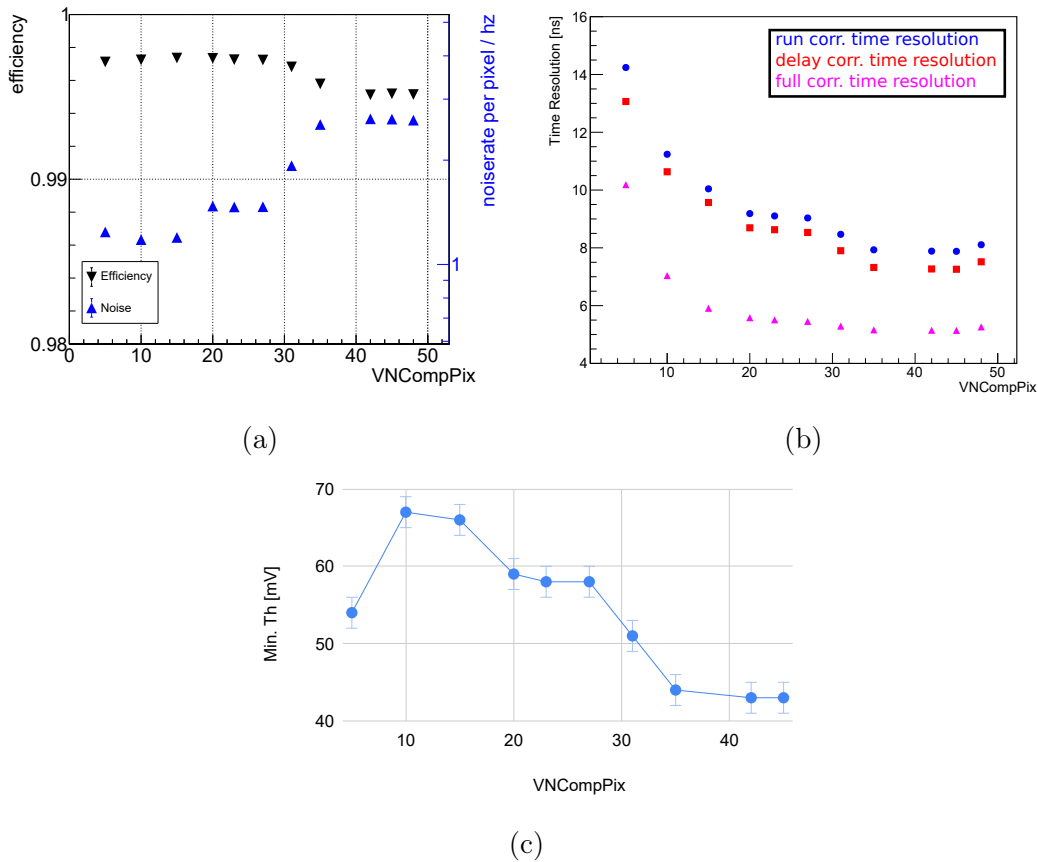


Figure 8.9: (a) Efficiency and noise rate, (b) time resolution, (c) minimum threshold for different VNCompPix values with an HV of -65 V

VNCompPix, which is the current of the source for the NMOS comparator, is characterized for values between 5 and 48. The tendency of the minimum threshold decreasing for higher VNCompPix is expected from the laboratory, except the drop for VNCompPix smaller than 10 (Chapter 7.2.6). The time resolution follows the minimum threshold behavior, even though, for VNCompPix higher than 40, the time resolution increases again.

The noise rate increases from 1 Hz to 3 Hz/pixel going to higher VNCompPix. The efficiency drops with VNCompPix higher than 31, however, the decrease is only around 0.1%. The superior time resolution motivates to choose VNCompPix between 33 and 42.

8.3.8 VNFBPix

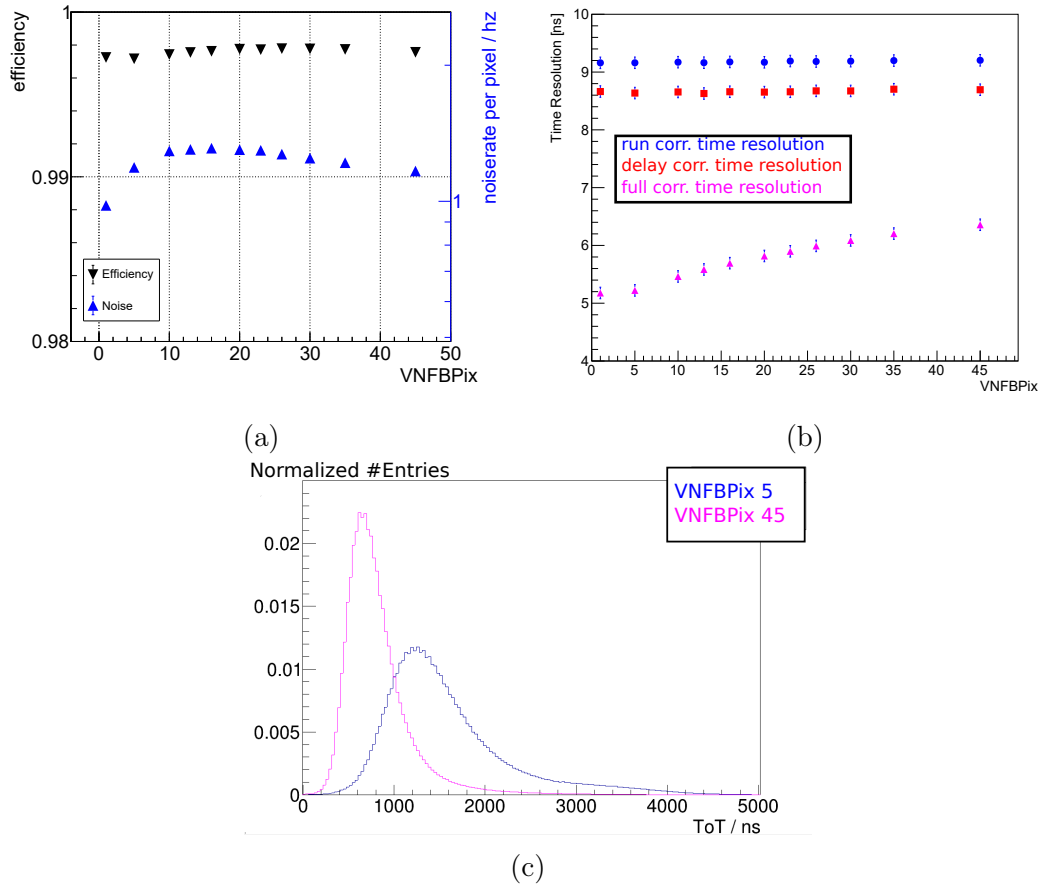


Figure 8.10: (a) Efficiency and noise, (b) time resolution, (c) normalized ToT spectrum for different VNFBPix values with an HV of -60 V

VNFBPix, which is the resistivity of the feedback, was measured with different characteristics in the laboratory and testbeam, see Chapter 7.2.7. The minimum threshold is not changing for different VNFBPix. The efficiency is stable for different VNFBPix values with a 0.03% fluctuation. Only the smallest noise rate is obtained for VNFBPix 2 with about 1 Hz/pixel. The run and delay corrected time resolutions are stable, but the full corrected time resolution increases for higher VNFBPix. The reason is that VNFBPix changes ToT spectrum (Figure 8.10 c). With higher VNFBPix, the ToT spectrum becomes sharper. The superior time resolution leads to a recommendation to use VNFBPix values between 1 to 10.

8.4 Time Resolution of the optimized Configuration

To obtain a good time resolution, the optimized configuration is chosen following the results of the DAC parameter scans in Chapter 8.3. The chosen values are described in Table 8.2.

VN [hex]	VNFB [hex]	VNComp [hex]	VGate [V]	VNLoad [hex]	VNFoll [hex]	VMinus [mV]	ckdivend2 [hex]
12	a	2a	2.08	a	7	700	7

Table 8.2: DAC setting for optimal time resolution

For the timing measurement, high voltage is set to -60 V (see Chapter 8.1). The minimum threshold for this configuration is about 44 mV. The efficiency is about 99.6 %, and the noise rate 1.9 Hz/pixel. Compared to the standard configuration, the efficiency is only 0.1 % smaller while the noise rate is about 0.8 Hz/pixel higher. For the single pixel timing analysis, a large number of runs have to be collected to obtain sufficient statistics.

8.4.1 Time Resolution of the Sensor

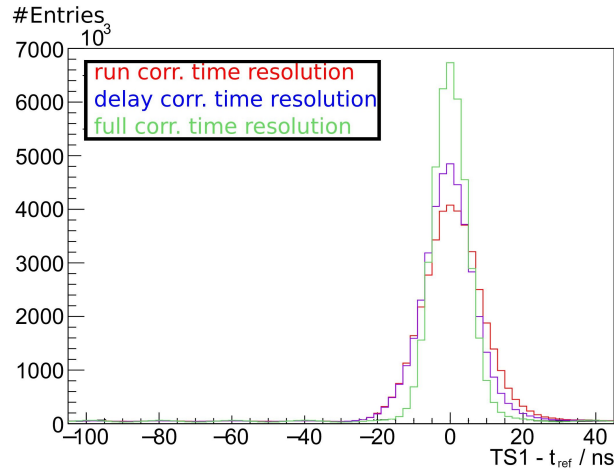


Figure 8.11: Time difference distributions for the ATLASPix3 sensor with the optimized configuration after different corrections.

Correction	Time Resolution [ns]	After binning correction [ns]
Run correction	8.0 ± 0.1	7.7 ± 0.1
delay correction	7.5 ± 0.1	7.1 ± 0.1
Full correction	5.1 ± 0.1	4.5 ± 0.1

Table 8.3: Time resolution for single pixel after different corrections. For the binning correction, the bin size of TS1 is 8ns.

The time difference distributions after run, delay and full correction are presented in Figure 8.11. In addition, the error of the time resolution is measured with the same method as for the testbema at DESY and the single setup. (Chapter 6.2.2 and 7.1)

In order to determine whether the chosen configuration is optimized, the full corrected time resolution is compared to the result at DESY. The measured time resolution at PSI is (4.5 ± 0.1) ns. This result is better than at the DESY campaign which was (5.0 ± 0.1) ns. The chosen configuration performs much better than the standard configuration from the laboratory and the settings used at DESY.

After delay correction, the time resolutions improve by 0.6 ns. And, the full corrected time resolution is improving by 2.5 ns. If the high voltage could be increased to -65 V, the run and delay corrected time resolution could be potentially improved even more, see Chapter 8.2.

8.4.2 Time Resolution of Single Pixel

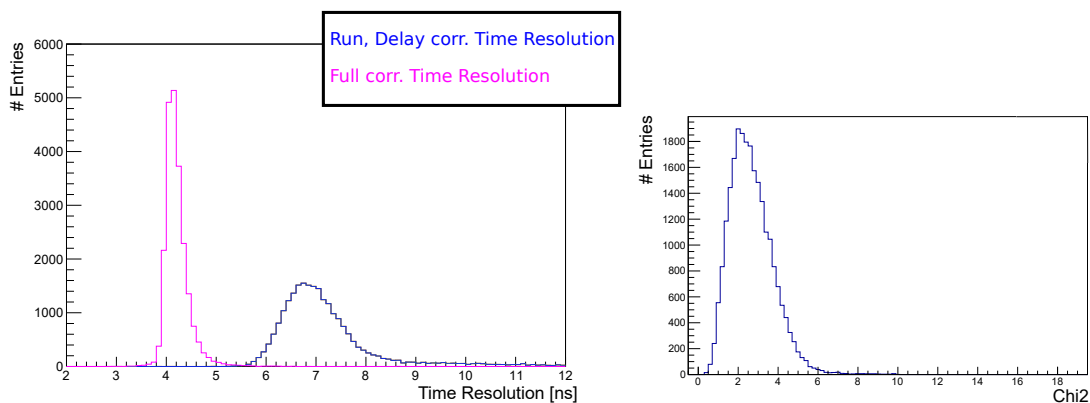


Figure 8.12: Time resolution distributions after different corrections. Run and delay corrected time resolution distributions are exactly the same, because only the mean of the time difference distributions is moved for the delay correction. The χ^2 distribution is from a Gaussian fit for time difference distributions of the pixels.

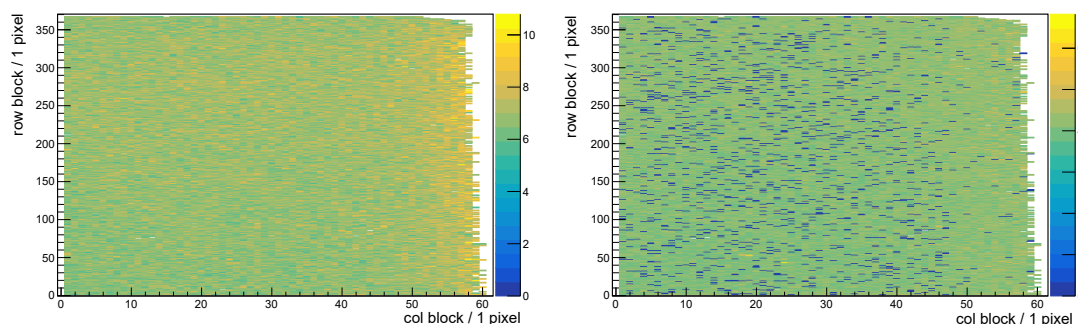


Figure 8.13: Time resolution maps: run and delay corrected (left), full corrected (right). Due to the edge effect of the chip and the beam position, the interesting region is limited by the number of entries.

Correction	Time Resolution [ns]	After binning correction [ns]
Run correction	6.7 ± 0.5	6.3 ± 0.5
delay correction	6.7 ± 0.5	6.3 ± 0.5
Full correction	4.1 ± 0.1	3.4 ± 0.1

Table 8.4: Time resolution for single pixels after different corrections. For binning correction, the bin size of TS1 is 8 ns.

The time resolution for single pixels is measured such that the time difference distribution for each pixel after different corrections is fitted with a range chosen to have always the same width. After fitting, the time difference distributions which have a

χ^2 higher than 10 are excluded. In addition, the pion beam does not cover all the active area of MuPix10 telescope and the ATLASPix3 sensor. Therefore, the pixels which have few number of hits are excluded for the timing analysis, For instance, the number of entries for the pixels has to be larger than 3000. In addition, the errors of the time resolution are defined as the standard deviation.

After run and delay correction, the time resolution distributions are identical because delay cannot be corrected for single pixel timing analysis.

The result of the time resolution for single pixels shows an enhanced time resolution compared to the testbeam result at DESY. The full corrected time resolution after binning correction is at (3.4 ± 0.1) ns compared to (3.7 ± 0.2) ns at DESY. The mean of the run and delay corrected time resolution is (6.3 ± 0.5) ns after binning correction for a high voltage of -60 V. If high voltage could be -65 V, this time resolution could be potentially ever smaller than 6 ns. After time walk correction, the mean of the time resolution is (3.4 ± 0.1) ns after binning correction for high voltage of -60 V. In this case, for a high voltage of -65 V, this time resolution could be enhanced as well.

9 Summary and Discussion

ATLASPix3 is the first full-scale prototype of an HV-MAPS with an active area of 3.7 cm^2 . It is designed to be used for multi-chip module production and for the use as a viable cost-efficient, low-material alternative to other types of pixel sensors typically used in high-energy physics experiments. This thesis focused on studying and optimizing the time resolution of ATLASPix3. In this context, several measurements were carried out in the laboratory as well as at two different testbeam campaigns. The delay and time walk correction applied in the offline timing analysis enhanced the time resolution. Further, a run-to-run offset was observed for the mean of the time difference distribution, which had to be corrected.

At the first chip test at DESY, where a high-energetic electron beam (3 GeV) was used, ATLASPix3 was tested for its time resolution and efficiency. This was done using a four-layer ATLASPix3 telescope. The time resolution for the single pixels analysis is $(6.9 \pm 0.6) \text{ ns}$ after run correction and $(3.7 \pm 0.2) \text{ ns}$ after the full correction. The high voltage was set to -60 V . The efficiency of the sensor was already at a high value of 99.7%.

The time resolution was then optimized in the laboratory by varying the DAC settings around the working point found at the DESY testbeam campaign. Sr-90 was used as a signal source and a scintillator for the reference time measurement.

Ultimately, the optimized settings and ranges have been tested in a second beam time at PSI (350 MeV pions, muons, and electrons). The coincidence signal of two scintillators was used as time reference. A telescope, consisting of three MuPix10 sensors, was used to perform efficiency measurements. The found standard configuration with the single setup in the laboratory was studied for its efficiency and time resolution. The results obtained with this standard configuration compared to the time resolution measured in the testbeam at DESY could only be improved slightly. So, a configuration for an optimized time resolution was investigated once more by DAC parameter scanning during this testbeam. For the final settings, an efficiency of 99.6% was obtained. The run corrected time resolution of the single pixels is $(6.3 \pm 0.5) \text{ ns}$ while the full corrected time resolution is $(3.4 \pm 0.1) \text{ ns}$ using a high voltage of -60 V . The result is enhanced compared to the results in the testbeam at DESY. Unfortunately, the current of the high voltage increased during this testbeam. So, the high voltage had to be decreased from -65 V to -60 V . Comparing the result for the high voltage of -60 V to -65 V with the standard configuration, the run corrected and delay corrected time resolutions are about 1 ns larger while the full corrected time resolution deviates by 0.4 ns. So, a high voltage of -65 V could enhance the time resolution even further with the configuration for the optimal time resolution.

The characterized ATLASPix3 shows in general a good performance. However, the minimum threshold is changing for different configurations. If the the threshold level could be reduced further, the time resolution could be enhanced. Comparing the DAC parameter scanning in the laboratory to the result in the testbeam, some parameters could not be optimized with the single setup, since high fluctuations are observed, but rather ranges could be defined that allow for a fast optimization on a testbeam campaign.

The results impressively show that knowledge from previous sensor prototypes, in this case ATLASPix1, can be easily transferred to find an efficient working point. Further, the performance limits achievable with this sensor prototype seem to be reached. To improve the time resolution further this has to be achieved by changes in the chip design, in the simplest case the increase of the break down voltage of the sensor diode.

10 Bibliography

- [1] W.N.Cottingham and D.A. Greenwood, *An Introduction to the Standard Model of Particle Physics (2ed edition)*, Cambridge University Press.
- [2] Carl D. Anderson, *The Apparent Existence of Easily Efectable Positives*, Science, **1932**, Vol.76.
- [3] The ATLAS Collaboration, *Observation of a new particle in the search for the Standard Model Higgs boson with the ATLAS detector at the LHC*, arXiv:1207.7214v2, **2012**.
- [4] ATLAS Collaboration. *Technical Design Report for the ATLAS Inner Tracker Pixel Detector*. Technical Report CERN-LHCC-2017-021. ATLAS-TDR030, CERN, Geneva, **Sep 2017**. URL: <https://cds.cern.ch/record/2285585>.
- [5] ATLAS main website <https://atlas.cern/discover/detector>, **31.Oct.2020**.
- [6] M. Tanabashi et al. (Particle Data Group), *Review of Particle Physics* Phys. Rev. D 98, 030001 – Published **17 August 2018**
- [7] Claus Grupen and Boris Shwartz, *Particle Detectors (2ed edition)*, Cambridge University Press, **2008**.
- [8] David Maximilian Immig, *Characterization of ATLASPix1, an HV-CMOS Demonstrator for the Phase-II Upgrade of the ATLAS Inner Tracker*, Master Thesis, Universität Heidelberg
- [9] Frank Hartmann, *Evolution of Silicon Sensor Technology in Particle Physics*, Springer, **2009**.
- [10] Leonardo Rossi, Peter Fischer, Tilman Rohe, Norbert Wermes, *Pixel Detectors From Fundamentals to Applications*, Springer, **2006**
- [11] Marius Grundmann, *The Phycsis of Semiconductors An Introduction Including Nanaphysics and Applications*, Springer, **2016**.
- [12] Hermann Kolanoski, Nobert Wermes, *Teilchendetektoren Grundlagen und Anwendungen*, Springer Spektrum, **2016**.
- [13] I. Peric, H. Augustin, *ATLASPIX3 user manual version 1*, **2019**.

- [14] Sebastian Dittmeier. *Fast data acquisition for silicon tracking detectors at high rates. Heidelberg, 2019.* doi:10.11588/heidok.00025791. URL: <http://nbn-resolving.de/urn:nbn:de:bsz:16-heidok-257910>.
- [15] David Maximilian Immig. *Charakterisierung des VCO, der PLL und der Pulsform des MuPix7 in Abhängigkeit der Umgebungstemperatur.* Bachelor Thesis, Heidelberg, **2016**.
- [16] Jan Patrick Hammerich, *Analog Characterization and Time Resolution of a large scale HV-MAPS Prototype,* Master Thesis, Universität Heidelberg, **2018**.
- [17] Deutsches Elektronen-Synchrotron, *Brief Description about Beam generation,* https://particle-physics.desy.de/test_beams_at_desy/e252106/e252211
- [18] Paul-Scherrer Institut, *$\pi M1$ Beamline,* <https://www.psi.ch/en/sbl/pim1-beamline>
- [19] Lennart Huth, *A High Rate Testbeam Data Acquisition System and Characterization of High Voltage Monolithic Active Pixel Sensors,* Heidelberg, **2018**.
- [20] N. Wermes, *Pixel Detectors,* 10.5170/CERN-2005-011.101, **2009**.
- [21] I. Peric. *A novel monolithic pixelated particle detector implemented in highvoltage CMOS technology.* Nucl.Instrum.Meth. A582, **2007**. doi: 10.1016/j.nima.2007.07.115
- [22] A. Blondel et al., *Research Proposal for an Experiment to Search for the Decay $\mu \rightarrow eee$.* (**Jan. 2013**). arXiv: 1301.6113 [physics.ins-det]
- [23] S. M. Seltzer and M. J. Berger. *Improved Procedure for Calculating the Collision Stopping Power of Elements and Compounds for Electrons and Positrons.* The International Journal of Applied Radiation and Isotopes, 35, **1984**
- [24] Ballabriga, Rafael, *The Design and Implementation in 0.13 μ m CMOS of an Algorithm Permitting Spectroscopic Imaging with High Spatial Resolution for Hybrid Pixel Detectors,* Barcelona : Ramon Llull U., Barcelona, **2009**
- [25] L. Mandok, *Analoge Charakterisierung und Optimierung des HV-MAPS Prototypen ATLASPix3,* Bachelor Thesis, Heidelberg, **2020**
- [26] A. Weber, H. Augustin, I. Peric, *MuPix10 Documentation,* Mu3e Internal Note 0052, **2020**
- [27] ROOT Data Analysis Framework, *Reference Guid,* <https://root.cern/doc/master/classTEfficiency.html>

Acknowledgments

For this master thesis, a lot of people helped and supported me in this year and last year.

First of all, I would like to thank Prof. André Schöning for giving me the huge opportunity to participate in this amazing group.

Thank you to the second examiner of my thesis, Prof. Ulrich Uwer.

A huge thanks to Heiko Augustin and David Maximilian Immig for supervising and supporting me during participation in the group and beyond.

I am deeply in debt to the people who reviewed my thesis:

Sebastian Dittmeier, Thomas Rudzki, Benjamin Weigl, Luigi Vigani, Heiko Augustin, David Maximilian Immig, Jan Hammerich, Adrian Herkert, Christof Sauer. Without your supporting, this thesis would be confusing.

I appreciate that I could work delightfully with all Mu3e and ATLAS groups members in Heidelberg. And the testbeam campaigns were the great experiences in my life.

To everyone who I have forgotten to mention here:

Sorry. But I feel thankful always.

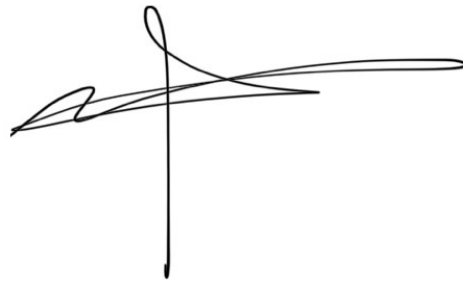
Last I want to thank my family and friends in Korea and Germany for unending support and love.

For my family and friends in Korea:

이 논문을 위해 응원하고 격려해준 가족과 친구들에게 감사의 인사를 드립니다.

Erklärung:

Ich versichere, dass ich diese Arbeit selbstständig verfasst habe und keine anderen als die angegebenen Quellen und Hilfsmittel benutzt habe.

A handwritten signature in black ink, consisting of several overlapping horizontal strokes and a vertical line extending downwards from the center.

Heidelberg, den 01.11.2020